



# Global analysis of the high resolution infrared spectrum of methane $^{12}\text{CH}_4$ in the region from 0 to $4800\text{ cm}^{-1}$

S. Albert<sup>a</sup>, S. Bauerecker<sup>a,b</sup>, V. Boudon<sup>c,\*</sup>, L.R. Brown<sup>d</sup>, J.-P. Champion<sup>c</sup>, M. Loëte<sup>c</sup>, A. Nikitin<sup>e</sup>, M. Quack<sup>a</sup>

<sup>a</sup>Physical Chemistry, ETH Zürich, CH-8093 Zürich, Switzerland

<sup>b</sup>Institut für Physikalische und Theoretische Chemie, Technische Universität Braunschweig, D-38106, Germany

<sup>c</sup>Institut Carnot de Bourgogne, UMR 5209 CNRS–Université de Bourgogne, 9 Av. A. Savary, BP 47870, F-21078 Dijon Cedex, France

<sup>d</sup>Jet Propulsion Laboratory, California Institute of Technology, 4800 Oak Grove Drive, Pasadena, CA 91109, USA

<sup>e</sup>Laboratory of Theoretical Spectroscopy, Institute of Atmospheric Optics, Russian Academy of Sciences, 634055 Tomsk, Russia

## ARTICLE INFO

### Article history:

Received 14 September 2008

Accepted 14 October 2008

Available online 1 November 2008

This paper is dedicated to Prof.  
W. Kutzelnigg in honor of his 75th birthday.

### Keywords:

Methane

High resolution infrared spectra

Line intensities

Vibrational states

Rovibrational analysis

## ABSTRACT

We report the global analysis of methane ( $^{12}\text{CH}_4$ ) lines from high resolution rovibrational spectra including accurate line positions and intensities in the region  $0\text{--}4800\text{ cm}^{-1}$ . This covers four polyads: The Ground State Monad (rotational levels), the Dyad ( $940\text{--}1850\text{ cm}^{-1}$ , 2 vibrational levels, 2 sublevels), the Pentad ( $2150\text{--}3350\text{ cm}^{-1}$ , 5 vibrational levels, 9 sublevels) and the Octad ( $3550\text{--}4800\text{ cm}^{-1}$ , 8 vibrational levels, 24 sublevels) and some of the associated hot bands (Pentad–Dyad and Octad–Dyad). New Fourier transform infrared (FTIR) spectra of the Pentad and Octad regions have been recorded with a very high resolution (better than  $0.001\text{ cm}^{-1}$  instrumental bandwidth, unapodized) at 78 K using the Bruker IFS 125 HR Zürich prototype (ZP2001) spectrometer in combination with a long optical path collisional cooling system [S. Albert, S. Bauerecker, M. Quack, A. Steinlin, *Mol. Phys.* 105 (2007) 541]. Existing spectra previously recorded with the FTIR spectrometer at the National Solar Observatory on Kitt Peak in Arizona were remeasured selectively to provide new intensities and positions of weaker lines above  $4400\text{ cm}^{-1}$ . These were combined with previously reported absorption data from FTIR and laser absorption, as well as high-resolution stimulated Raman and microwave spectra. The effective hamiltonian was expanded up to order 6 for the Ground State, order 6 for the Dyad, order 5 for the Pentad and order 5 for the Octad. A total of 16,738 line positions were used in the least squares adjustment characterized by the following global root mean square deviations  $d_{\text{RMS}}$  for line positions:  $1.3 \times 10^{-4}\text{ cm}^{-1}$  for the Dyad,  $6.0 \times 10^{-4}\text{ cm}^{-1}$  for the Pentad, and  $3.5 \times 10^{-3}\text{ cm}^{-1}$  for the Octad. Absolute intensities were also analyzed for all the cold bands and some of the hot bands in the region under consideration and we obtained  $d_{\text{RMS}} = 9.6\%$  including 3262 experimental line intensities for the Octad. This analysis represents a large improvement over the previous one [J.-C. Hilico, O. Robert, M. Loëte, S. Toumi, A.S. Pine, L.R. Brown, *J. Mol. Spectrosc.* 208 (2001) 1] with  $d_{\text{RMS}} = 0.041\text{ cm}^{-1}$  for positions and 15.6% for intensities in the Octad for a smaller data set. The new results are discussed as benchmarks in relation to accurate potential energy hypersurfaces and for atmospheric and planetary spectra.

© 2008 Elsevier B.V. All rights reserved.

## 1. Introduction

Methane ( $\text{CH}_4$ ) is the prototypical hydrocarbon, which is important in numerous fields of science. One may name here its fundamental role in the history of our understanding of three dimensional molecular structures and chemical bonding [1–3], leading today to the formulation of accurate potential energy hypersurfaces for molecular quantum dynamics [4–9]. The methane molecule has been an important example for studies of time dependent intramolecular quantum wavepacket dynamics [10,11]

as well as an example for fully 9-dimensional calculations of time independent vibrational quantum eigenstates [12]. Methane has also been repeatedly used as testing ground for accurate *ab initio* electronic structure calculations [13–15].  $\text{CH}_4$  has been a classic case for the study of nuclear spin symmetry conservation [16]. The subtle balance of electric dipole moments leading to the small electric dipole moment of methane isotopomers  $\text{CH}_3\text{D}$ ,  $\text{CH}_2\text{D}_2$  and  $\text{CHD}_3$  has been a long standing problem [17–23] resolved only recently [4,5,17]. At the most fundamental level, the possible role of the parity violating electroweak interaction in relation to methane stereomutation has been discussed as well [24–26].

Towards more applied sciences, methane plays a crucial role in fields such as geosciences, reaction kinetics and combustion

\* Corresponding author. Tel.: +33 0 3 80 39 59 17; fax: +33 0 3 80 39 59 71.  
E-mail address: [Vincent.Boudon@u-bourgogne.fr](mailto:Vincent.Boudon@u-bourgogne.fr) (V. Boudon).

science, chemical technology of hydrogen generation, biotechnology, astrophysics, atmospheric and environmental science to name but a few. On Earth, CH<sub>4</sub> is the main constituent of natural gas and excepting H<sub>2</sub>O it is the second most important greenhouse gas (after carbon dioxide) responsible for the present global warming, as established in Annex B of the Kyoto protocol and demonstrated by many studies [27]. CH<sub>4</sub> is also an important constituent of various planetary atmospheres, like those of the Giant Planets (Jupiter [28,29], Saturn [30], Uranus [31] and Neptune [32]), of Titan (Saturn's main satellite) [33–37], Triton (Neptune's main satellite) and Pluto [38]. It is even suspected to be present in Mars' atmosphere [39]. It is also likely to be abundant in some of the newly-discovered extrasolar planets (the so-called “hot jupiters”) and brown dwarfs. As a matter of fact, the discovery of methane in the atmosphere of exoplanet HD 189733b has been reported very recently [40].

Since infrared spectroscopy is generally the best diagnostic tool to study CH<sub>4</sub> in these environments, it appears essential to be able to model its absorption very precisely. This is true for the study of methane itself (*i.e.* its distribution, sources and sinks) but also for the determination of physical conditions, chemistry, optical properties and minor constituents of planetary atmospheres. A striking example is Titan which is presently studied by the Cassini–Huygens mission [33–37]. CH<sub>4</sub> is present in significant amounts (a few %) on Titan at temperatures reaching around 80 K and thus the strong absorption bands make its atmosphere almost opaque, the ground being visible from space only through the methane transparency windows [36,37]. A correct interpretation of Titan's images, as well as the study of the many minor compounds responsible for its complex hydrocarbon chemistry, require first a global modeling of infrared absorption of CH<sub>4</sub>.

The vibrational spectroscopy of methane has been studied for a long time [41–43]. Due to the high-symmetry of the molecule and the related polyad structure of close lying levels [44] it is quite complex. Indeed, the four normal mode frequencies  $\nu_i$  of CH<sub>4</sub> exhibit an approximate relation of stretching and bending frequencies with  $\nu_1 \approx \nu_3 \approx 2\nu_2 \approx 2\nu_4$  resulting in vibrational levels being grouped into polyads with levels of similar energy. The number of interacting vibrational levels within each polyad increases rap-

idly with the polyad number, making the line-by-line assignment analysis more and more difficult when progressing toward the near infrared regions and above.

Fig. 1 shows a survey of the polyad energy level scheme for <sup>12</sup>CH<sub>4</sub> including a definition of the nomenclature. In the convention used here, the polyads  $P_n$  are simply numbered with increasing energy starting with  $n = 0$  for the Monad,  $n = 1$  for the Dyad *etc.* In this nomenclature the polyad number  $n$  gives roughly the number of CH-bending quanta with pure bending excitation and  $n/2$  roughly the number of CH-stretching quanta with pure stretching excitation. In an alternative nomenclature in the literature one uses the polyad quantum number  $N = n/2$ , where one has then also polyads with half odd integer index [45]. Fig. 1 shows also the number of levels and sublevels within each polyad labeled with Greek prefix for the number of levels (Monad for 1, Dyad for 2 *etc.*). The number of levels is obtained from counting simply harmonic oscillator excitations with possible combinations of quanta in the modes. However, starting with the Pentad, these levels split into a larger number of vibrational sublevels of well defined symmetry species in the point group  $T_d$  ( $A_1$ ,  $A_2$ ,  $E$ ,  $F_1$ ,  $F_2$ ), 9 sublevels for the Pentad and 24 for the Octad, see Section 3.1 below). Finally one might also count the number of non-degenerate vibrational states by giving each sublevel a degeneracy corresponding to its species (1 for  $A$ , 2 for  $E$  and 3 for  $F$ ). This would be relevant for the approximate average total vibrational density of states which is roughly the number of states in the polyad divided by the polyad width, by definition less than a bending quantum if the polyads are separated. This is relevant in statistical mechanics and kinetics. In many applications, however, the density of vibrational states of a given symmetry species including total parity are relevant [46–48].

The Ground State Monad of <sup>12</sup>CH<sub>4</sub> has been known for a long time from its centrifugal distortion spectrum in the microwave (Q branch) and THz (R branch) regions [49–53]. Intensities in the THz region have been recently reinvestigated [54]. The Dyad 1100–1800 cm<sup>−1</sup> region is now also very well understood [55,56], including line positions and intensities and also many studies concerning lineshapes, *e.g.* [57,30]. The Pentad from 2300 to 3300 cm<sup>−1</sup> region has been modeled with high accuracy by Hilico et al. [58]. The Octad from 3500 to 4700 cm<sup>−1</sup> has been stud-

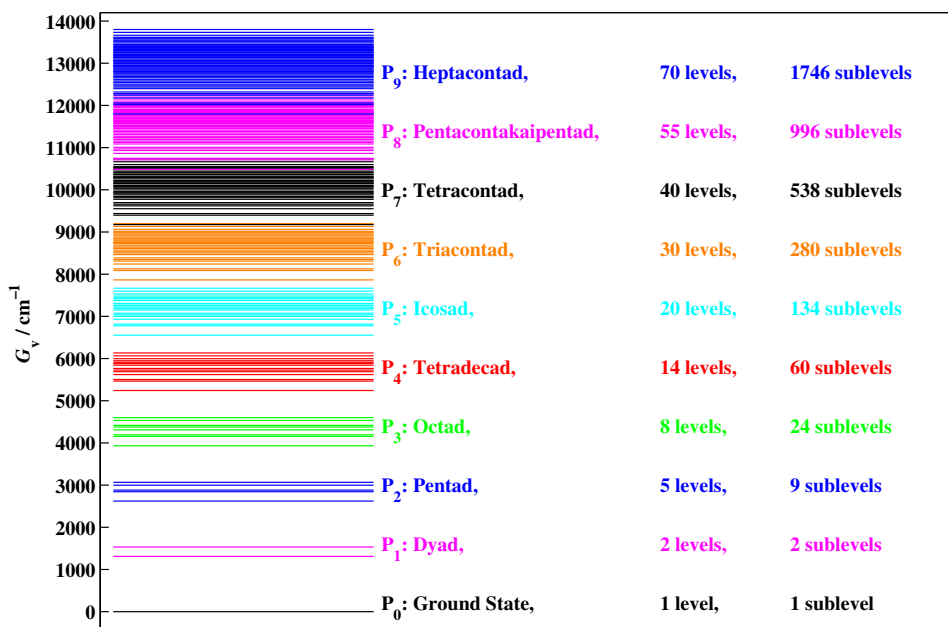


Fig. 1. The vibrational polyads of methane. The ordinate gives the vibrational term value  $G_v$  measured from the Ground State zero point level (color online). (For interpretation of the references to color in this figure legend, the reader is referred to the web version of this article.)

ied in a preliminary analysis [59]. Nevertheless, the modeling of this region, which is very important especially for planetary applications, has been insufficiently precise, with a global root mean square deviation  $d_{\text{RMS}}$  for line positions of  $0.041 \text{ cm}^{-1}$ , which is quite high considering the usual high resolution spectroscopic standards. Moreover, the strategy employed to interpret the complex near infrared spectrum of methane is to build upon the analysis and results of the low vibrational bands. For this we use retrieved constants of a successfully modeled lower polyad to predict the structure expected for the next higher set of states. Through successive analyses, we then construct a polyad ladder that will permit the very complex regions at shorter wavelengths to be understood. The  $4800\text{--}6300 \text{ cm}^{-1}$  region of the Tetradead, also of primary importance for many applications, has been analyzed only partially up to now [60], and its detailed investigation awaits for a fully reliable hamiltonian parameter set for the polyads below it. Highly accurate cw-CRD (cavity ring down) supersonic jet spectra of the Icosad [61] around  $7500 \text{ cm}^{-1}$  exist already. Although some localized structure of prominent bands can be assigned, even a preliminary analysis will require considerable effort. Finally we should also mention that measured positions and intensities to up to  $9200 \text{ cm}^{-1}$  are available (i.e. through the Triacontad [62]).

Given the importance of the topic in relation to the questions mentioned above, it is the goal of the present work to provide a essentially definitive global analysis of the infrared spectrum of methane in the complete range from 0 to  $4800 \text{ cm}^{-1}$  covering all polyads up to and including the Octad. The basis for this analysis is provided by new highly accurate experimental results obtained from the Zürich prototype (ZP2001) Bruker IFS 125 HR spectrometer in combination with an enclosive flow cooling cell, providing reduced Doppler widths at 78 K. These new results provide about 1400 accurate line positions and are combined with various existing line positions (about 11,800 data) and intensities (almost 4000 lines). The highly accurate parameters of the effective hamiltonian resulting from a global least squares adjustment to the complete data set will provide benchmark data for full-dimensional quantum calculations [63,64] improving finally potential energy hypersurfaces [9]. Furthermore, they can be used for reliable simulations of methane spectra under a variety of conditions ranging from planetary atmospheres to flames. In addition, they enable improved statistical mechanical partition function calculations in view of thermodynamical ideal gas properties [65] or for improved

calculations of statistical kinetics [66,67]. Finally, complete and reliable calculations of methane line intensities and frequencies based on the present work will improve the remote sensing of the terrestrial and planetary atmospheres.

The present work will also be a reliable starting point for traceable analysis of the  $^{12}\text{CH}_4$  Tetradead and Icosad spectra. As mentioned above, highly accurate measurements exist already but with only very preliminary analyses [61,68]. A preliminary account of parts of the present global analysis had been given in [69].

Section 2 describes the various experimental data sets used in the present study. Section 3 recalls the theoretical model used for methane. In Sections 4 and 5, we present the results of the new fits for line positions and intensities, respectively, and discuss them in Section 6.

## 2. Experimental data

Table 1 provides for convenience a summary of available spectroscopic data relevant for the present work on  $^{12}\text{CH}_4$ . These include new experimental results based on the Zürich cooling cell-FTIR experiments [70]. We shall in the following describe the new measurements of the present work, as well as the other data used in the analysis, partly available from the literature cited. This will provide a concise summary of the complete database used. The line frequencies and intensities used in the least squares adjustment as well as the corresponding quantities calculated from the effective hamiltonian resulting from a global least squares adjustment can be found in the tables of the Appendix published as Supplementary material [71].

### 2.1. New high-resolution spectra in the Pentad and Octad regions at 78 K

The cold cell FTIR spectra of  $\text{CH}_4$  and its isotopomers  $^{13}\text{CH}_4$ ,  $\text{CH}_3\text{D}$ ,  $\text{CH}_2\text{D}_2$  and  $\text{CD}_3\text{H}$  were measured at 78 K in a collisional and enclosive cooling cell system described in detail in [70] designed as a multireflection White-type cell [72]. Table 2 shows the measurement conditions. The cooling cell is connected via an evacuable transfer optics chamber to the external parallel port of the Zürich 2001 prototype of the IFS125 Bruker spectrometer allowing for a maximum optical path difference (MOPD) of 10 m in the interferometer [73–75] with a best possible bandwidth (FWHM, unapodized) of about

**Table 1**  
Experimental overview of  $^{12}\text{CH}_4$  infrared measurements used.

	Dyad and Pentad–Dyad region	Pentad and Octad–Dyad region		Octad region	
		Previous work	New cold data	Previous work	New cold data
Spectral range covered/ $\text{cm}^{-1}$	1100–2600 [56]	1800–5500 [58,84,85,113,109]	2750–5600	1800–5500, 3500–7300 [80,114,115,59,62]	2750–7800
Unapodized resolution/ $\text{cm}^{-1}$ (instrum. band width FWHM)	0.0056, 0.011 [56]	0.011 [58,109], 0.0004 [85,113,109]	0.0027–0.004	0.011 [80,114,115,59,62]	0.004–0.005
# of spectra for line intensities	24 [82]	14 [84,85,113,109]		14 [80,114,115,59,62]	
Path length/m	0.027–433 [56]	0.05–433 [58,109]	5–10	0.25–433, 8.3–40.3 [80,114,115,59,62]	5–10
Pressure/ torr <sup>a</sup>	0.3–19.5 [56]	0.41–10.1 [84,85,113,109]	2.1–4.3	3.4–17, 0.1–1.0	2.1–4.3
Exp. uncertainties of intensities for unblended assigned lines	3% [81,83]	3% [58,84,85,113,109]		3% [80,114,115,59,62]	
Calibration	$\text{H}_2\text{O}$ [116]	$\text{CH}_4^b$ [117] $\text{CO}$ [118]	$\text{CH}_4$ , $\text{H}_2\text{O}$ [78]	$\text{CO}$ , $\text{N}_2\text{O}$ [118,119]	$\text{CH}_4$ , $\text{H}_2\text{O}$ [78]
Exp. uncertainties of line positions for unblended lines/ $\text{cm}^{-1}$	0.00008 [56]	0.0002 [58,109]	Absolute 0.0001 [78] Relative 0.000001 <sup>c</sup>	0.0002 [80,114,115,59,62]	Absolute 0.0001 [78] Relative 0.000001 <sup>c</sup>
Temperature/K	298–305 [56]	298–305 [58,84,85,113,109]	78	298 [80,114,115,59,62]	78
# of positions used	2610	6135	–	11,842	1386

<sup>a</sup> 1 Torr  $\approx 133.322 \text{ Pa}$  [79].

<sup>b</sup> P branch of  $\nu_3$  using [117]; J. W. Brault, private communication.

<sup>c</sup> This work.

**Table 2**Experimental details for the cold sample spectra of  $^{12}\text{CH}_4$ .

Region <sup>a</sup> $\tilde{\nu}/\text{cm}^{-1}$	Res. $\delta\tilde{\nu}/\text{cm}^{-1}$	Source	Opt. filter $\delta\tilde{\nu}_{\text{opt}}/\text{cm}^{-1}$	Apert./mm	$\nu_{\text{mir}}/\text{kHz}$	El. filter $\delta\tilde{\nu}_{\text{el}}/\text{cm}^{-1}$	Path l/m	$p^b/\text{Pa}$	# scans coadded	T/K
2900–3700	0.0027	Globar	3000–3600	1.0	40	2370–3950	5	570	100	78
3200–4600	0.0033	Tungsten	3350–4450	1.0	40	2765–5529	5	460	117	78
4200–5600	0.0040	Tungsten	4350–5500	1.0	40	2765–7109	10	280	120	78
5200–6400	0.0047	Tungsten	5350–6350	1.0	40	3950–7109	10	280	200	78
6200–8100	0.0050	Tungsten	6250–8000	0.8	40	3950–13823	10	290	160	78

<sup>a</sup> All experiments summarized here used KBr windows, Si:CaF<sub>2</sub> beamsplitter and liquid nitrogen cooled InSb detector.<sup>b</sup> Pressure of a mixture of CH<sub>4</sub> and He.

0.0007  $\text{cm}^{-1}$ . The FTIR spectrum of CH<sub>4</sub> has been recorded in four different regions ranging from 2750 to 8000  $\text{cm}^{-1}$ . The nominal resolution, defined as 1/MOPD (maximum optical path difference) ranged from 0.0027  $\text{cm}^{-1}$  at 3000  $\text{cm}^{-1}$  to 0.005  $\text{cm}^{-1}$  at 8000  $\text{cm}^{-1}$ . Apertures between 0.8 and 1.0 mm were used. The actual instrumental bandwidth (FWHM, unapodized) is somewhat smaller than this nominal bandwidth [74].

The temperature and the pressure can be independently adjusted between 4 and 400 K and between 0.01 and 3000 mbar with the cooling system used in the present work. This covers atmospheric and many extraterrestrial basic conditions. The collisional cooling cell can be operated in different modes. The simplest is the static mode. A coolant such as liquid nitrogen is filled into the Dewar vessel and cools the cell to a fixed temperature. In the vapor pressure limited mode, the cell temperature is exactly adjusted by heating corresponding to the desired pressure of the sample. Further, in the enclosive flow mode the sample gas is continuously injected into the cell while the buffer gas flows radially from the whole inner cell wall into the cell, and minimizes wall contacts of the sample gas [76,77].

In the present investigation the collisional cooling cell was used in the static mode with liquid nitrogen as coolant. The CH<sub>4</sub> spectra shown in Figs. 2, 4 and 5 were taken at 78 K (as most of the spectra used here) with path lengths ranging from 5 to 10 m. The sample pressures of the mixtures of CH<sub>4</sub> and helium ranged from 280 to 570 Pa where the CH<sub>4</sub> pressure was kept around 40 Pa. Pressure broadening can be neglected under these conditions. All spectra were self-apodized and were recorded with instrumental widths below the Doppler widths ranging from 0.0046  $\text{cm}^{-1}$  at 78 K and 2900  $\text{cm}^{-1}$  to 0.0123  $\text{cm}^{-1}$  at 78 K and 7800  $\text{cm}^{-1}$ . Table 2 shows the measurement parameters. The relative wavenumber uncertainty of the line positions is  $10^{-6}$  for the Bruker IFS 125 Zurich prototype 2001 spectrometer. In order to obtain the absolute wavenumber accuracy the spectra were calibrated with CH<sub>4</sub> and H<sub>2</sub>O line positions from the HITRAN database [78]. The absolute wavenumber accuracy is estimated to be better than 0.0001  $\text{cm}^{-1}$ . Fig. 2 provides a survey of the cold spectra.

## 2.2. Intensity measurements in the Octad region

In the study of Hilico et al. [59], 7930 Octad positions and 2506 line intensities were selected from a set of retrievals for over 6000 spectral lines between 3700 and 4700  $\text{cm}^{-1}$ . However, no assignments were known for several hundred isolated lines. The improvement of the Octad prediction permitted

1. the assignment of several hundred existing measurements and
2. new retrievals specifically targeting weaker transitions of under-represented bands and higher  $J$  values in crowded portions of the spectrum.

Most of the new values were found above 4400  $\text{cm}^{-1}$  and had line intensities below  $2.5 \times 10^{-4} \text{ cm}^{-2} \text{ atm}^{-1}$  at 296 K (see [79] for various conversions to other intensity units). In all, more than 800

new Octad intensities were added to the master collection. It should be noted that the most recent re-measured stronger lines of the Octad reported by Predoi-Cross et al. [80] and unpublished weaker lines from Brown [62] are not included in the present analysis. These might be considered when a future improvement in the model can be achieved, but we do not expect substantial changes from including these data.

## 2.3. Other sources of experimental data

During the last 30 years, the infrared spectrum of methane has been examined using numerous high resolution spectra recorded with FTIR and laser spectrometers. With high signal to noise data and retrievals being done by curve-fitting (e.g. [81]), the resulting observed values for the well-isolated transitions were of sufficient accuracies (better than 0.0004  $\text{cm}^{-1}$  for positions and 3% for line intensities) to motivate better theoretical modeling. In Table 1, we give a general overview including previously collected  $^{12}\text{CH}_4$  positions and line intensities still available electronically for the Dyad, Pentad and Octad regions.

### 2.3.1. Infrared line positions and intensities

The majority of the line positions and intensities in the infrared were obtained at room temperatures with the FTS located at the National Solar Observatory on Kitt Peak in Arizona. Altogether, more than 20,000 lines were measured by curve-fitting. Of these, some 1700 Dyad and Pentad–Dyad transitions were selected for modeling, while over 6000 transitions were included for the Pentad and Octad–Pentad bands. The data for the Octad region were discussed in Section 2.2. The Kitt Peak FTS data were obtained at lower resolution but because of the higher temperature each spectrum covered a wider spectral interval with sufficient overlap to check the internal consistency of line positions and intensities for the three polyads.

The accuracies of the line positions were limited by the signal to noise ratio of the spectra and the combination of room temperature Doppler widths and instrumental widths. The signal to noise ratio of the Dyad data was often 300:1 because Ar-doped Si detectors were used. Better signal to noise ratios were obtained using InSb detectors in both the Pentad and Octad regions, but the increasing Doppler widths, higher instrumental bandwidths (0.01  $\text{cm}^{-1}$  rather than about 0.005  $\text{cm}^{-1}$ ) and increasing complexity and density of the spectrum resulted in accuracies that varied from 0.0001  $\text{cm}^{-1}$  to 0.0030  $\text{cm}^{-1}$ .

The accuracies of line intensities were thought to be 3% or better for stronger well isolated features, but the quality degraded rapidly for blended lines. Efforts were made to filter out the worst values and retain lines good to at least  $\pm 10\%$ , although measurements with slightly poorer accuracies were included for the very weakest sublevels of the Octad. Further details can be seen in the original publications [59,80–83].

Additional values were taken from the laser studies by Pine who provided intensities of the allowed  $\nu_3$  transitions [84,85]. In addition, spectra at room temperature and at low temperature were re-

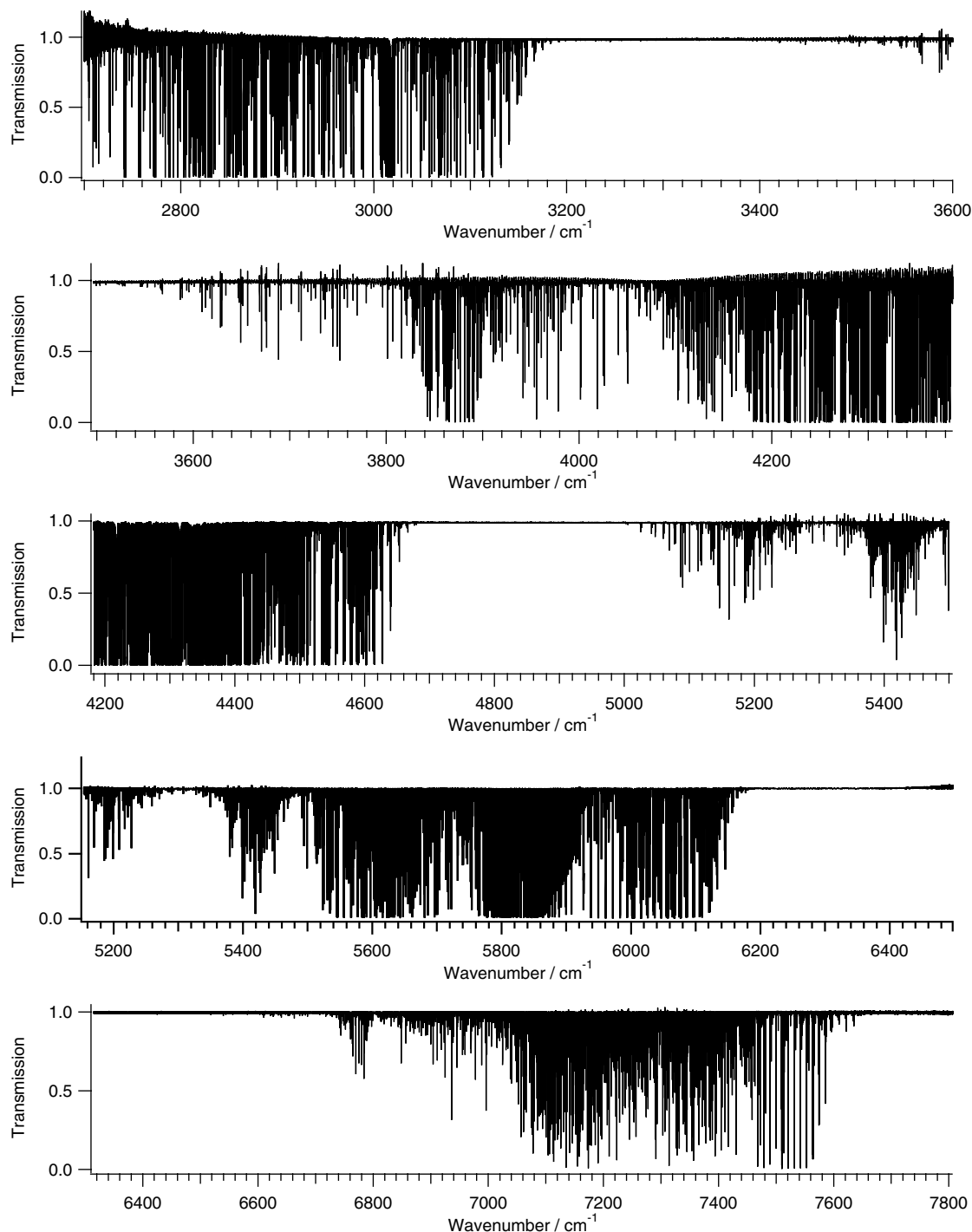


Fig. 2. Overview spectra of  $^{12}\text{CH}_4$  in the region 2750–7800  $\text{cm}^{-1}$  recorded at 78 K (ETH spectra).

ported for the  $3\nu_4$  band [59] which provided line positions, intensities and estimated lower state energies. These line intensities were thought to be accurate to 1%.

Finally, line parameters for  $R(17)$  through  $R(22)$  of  $\nu_3$  were measured by Grigoriev et al. [86] who used a Bruker HR 120 FT spectrometer; the accuracies of these line positions and intensities were estimated to be 0.0005  $\text{cm}^{-1}$  and 3%, respectively, for unblended lines.

### 2.3.2. Raman line positions

We used 146 Raman line positions in the Pentad region (they are in fact lines from the  $\nu_1$  fundamental band). They consist either

in stimulated Raman lines from the Madrid group [87] or in CARS lines from the Dijon group [88].

### 2.3.3. Microwave line positions

We also included in the fit some rotational microwave data in different vibrational states:

1. In the Ground State (GS–GS transitions) we used 37 lines from Oldani et al. [89] and 8 unpublished lines from Dreizler [90].
2. In the  $\nu_4 = 1$  state (Dyad–Dyad transitions), we used 14 lines from Hilico et al. [91] and 6 lines from Oldani et al. [53].



3. In the  $v_3 = 1$  state (Pentad–Pentad transitions), we used 15 lines from Pursell and Weliky [92] and 2 lines from Takami et al. [93] just as it was already done in Ref. [58] for the analysis of the Pentad system alone.

The small number of these rotational lines is compensated by their high precision, as will be discussed later. In the global fit presented below, these data mainly determined the Ground State tetrahedral constants (but the infrared data also contributed to the fit of the Ground State scalar constants).

### 3. Theory

#### 3.1. The polyads of methane

As all  $XY_4$  tetrahedral molecules, methane has four normal modes of vibration. They can be labeled by irreducible representations (irreps) of the  $T_d$  point group, according to the symmetry of the associated normal coordinates. We have thus:  $v_1(A_1)$ ,  $v_3(F_2)$  (stretching modes),  $v_2(E)$  and  $v_4(F_2)$  (bending modes).  $v_1(A_1)$  is a non-degenerate oscillator, while  $v_2(E)$  is doubly degenerate and  $v_3(F_2)$  and  $v_4(F_2)$  are triply degenerate. The fundamental frequencies exhibit a simple approximate relation,

$$v_1(A_1) \simeq v_3(F_2) \simeq 2v_2(E) \simeq 2v_4(F_2) \quad (1)$$

which leads to a well-defined polyad structure, with each polyad  $P_n$  defined by the integer  $n$  as

$$n = 2(v_1 + v_3) + v_2 + v_4, \quad (2)$$

where the  $v_i = 0, 1, 2, \dots$  ( $i = 1-4$ ) are the vibrational quantum numbers.  $P_0$  is the Ground State (GS) – or Monad. Each set  $(v_1, v_2, v_3, v_4)$  defines a *vibrational level*. Due to the degeneracy of three of the normal vibrations, each vibrational level contains a certain number of *vibrational sublevels*, whose symmetries can be found by means of group theoretical methods [43]. For instance, in polyad  $P_2$ ,  $v_2 + v_4$ , i.e. the  $(0, 1, 0, 1)$  level has two sublevels, since  $E \otimes F_2 = F_1 \oplus F_2$ ; in polyad  $P_4$ , the  $v_2 + v_3 + v_4$ , i.e. the  $(0, 1, 1, 1)$  level has eight sublevels, since  $E \otimes F_2 \otimes F_2 = A_1 \oplus A_2 \oplus 2E \oplus 2F_1 \oplus 2F_2$ , etc. Fig. 1 shows schematically the first 10 polyads of  $CH_4$  with the number of interacting vibrational levels and sublevels for each of them.

#### 3.2. Tensorial model for the hamiltonian

The theoretical model used in this paper is based on the tetrahedral tensorial formalism and the vibrational extrapolation methods developed in Dijon. These methods have already been explained, for example, in Refs. [94–99], and the reader should refer to these publications for details concerning notations and operator constructions. We wish here, however, to stress the main characteristics of this approach.

Let us consider an  $XY_4$  molecule for which the vibrational levels are grouped in a series of polyads  $P_k$  ( $k = 0, \dots, n$ ) as defined above. Consequently, we assume that intra-polyad interactions are strong and should be treated exactly, while inter-polyad interactions can be considered as small perturbations. After performing contact transformations in order to eliminate inter-polyad interactions, the resulting effective hamiltonian operator can be put in the following form:

$$\tilde{\mathcal{H}} = \tilde{\mathcal{H}}_{\{P_0\}} + \tilde{\mathcal{H}}_{\{P_1\}} + \dots + \tilde{\mathcal{H}}_{\{P_k\}} + \dots, \quad (3)$$

where each  $\tilde{\mathcal{H}}_{\{P_k\}}$  term contains rovibrational operators which have vanishing matrix elements within the  $P_{k' < k}$  basis sets and is expanded in the form

$$\tilde{\mathcal{H}}_{\{P_k\}} = \sum_{\text{all indices}} \tilde{t}_{\{s\}\{s'\}}^{\Omega(K,n\Gamma)F_v\Gamma_v} T_{\{s\}\{s'\}}^{\Omega(K,n\Gamma)F_v\Gamma_v}. \quad (4)$$

In this equation the  $\tilde{t}_{\{s\}\{s'\}}^{\Omega(K,n\Gamma)F_v\Gamma_v}$  are the effective hamiltonian parameters to be determined by fitting experimental line positions and the  $T_{\{s\}\{s'\}}^{\Omega(K,n\Gamma)F_v\Gamma_v}$  are rovibrational operators defined as

$$T_{\{s\}\{s'\}}^{\Omega(K,n\Gamma)F_v\Gamma_v} = \beta \left[ \varepsilon V_{\{s\}\{s'\}}^{\Gamma_v\Gamma_v\Gamma_v} \otimes R^{\Omega(K,n\Gamma)} \right]^{(A_1)}, \quad (5)$$

where  $\beta$  is a numerical factor equal to  $\sqrt{3}(-\sqrt{3}/4)^{\Omega/2}$  if  $(K,n\Gamma) = (0, 0A_1)$ , and equal to 1 otherwise (this is used to let the low order parameters match the “usual” notation, like  $\tilde{t}_{\{0\}\{0\}}^{2(0,0A_1)A_1A_1} \equiv B_0$  for the  $J^2$  term in  $\tilde{\mathcal{H}}_{\{P_0\}}$ , etc). As shown by Eq. (5), the rovibrational operators  $T_{\{s\}\{s'\}}^{\Omega(K,n\Gamma)F_v\Gamma_v}$  are obtained by the totally symmetric coupling of a rotational operator  $R^{\Omega(K,n\Gamma)}$  with a vibrational operator  $\varepsilon V_{\{s\}\{s'\}}^{\Gamma_v\Gamma_v\Gamma_v}$ .

Vibrational operators  $\varepsilon V_{\{s\}\{s'\}}^{\Gamma_v\Gamma_v\Gamma_v}$  are constructed by recursive couplings of elementary creation ( $a^+$ ) and annihilation ( $a$ ) operators for each normal mode.  $\varepsilon = \pm 1$  is the parity under time reversal. In practice, different construction rules are possible. The coupling scheme used in the STDS software [100] is described in Ref. [96]; the one used in the MIRS software is described in Ref. [98]. Operators in both schemes can be deduced from each other through linear unitary transformations. Let us call  $\Omega_v$  the degree in  $a$  or  $a^+$  operators. Rotational operators  $R^{\Omega(K,n\Gamma)}$  are also built recursively from successive couplings of the elementary tensor  $R^{1(1)} = 2J$  using the method of Moret-Bailly [101,102] and Zhilinskii [103]. They are symmetrized using the  $O(3) \supset T_d$  orientation matrix defined in [104,105].  $\Omega$  is the degree in  $J_x, J_y$  or  $J_z$  operators and we have thus necessarily:

$$\varepsilon = (-1)^\Omega, \quad (6)$$

so that each hamiltonian operator in Eq. (5) is invariant under time reversal. The order of each individual term in Eq. (5) is defined as

$$\mathcal{O}_H = \Omega + \Omega_v = 2. \quad (7)$$

The effective hamiltonian for polyad  $P_n$  is obtained by projecting  $\tilde{\mathcal{H}}$  in the  $P_n$  Hilbert subspace, i.e.,

$$\tilde{H}^{(P_n)} = P^{(P_n)} \tilde{\mathcal{H}} P^{(P_n)} = \tilde{H}_{\{P_0\}}^{(P_n)} + \dots + \tilde{H}_{\{P_k\}}^{(P_n)} + \dots + \tilde{H}_{\{P_n\}}^{(P_n)}. \quad (8)$$

This corresponds to the so-called “vibrational extrapolation”: the effective hamiltonian for a given polyad contains all the parameters for the lower polyads. This kind of “encapsulation” of the effective hamiltonian parameters has some important consequences:

1. One can analyse molecular spectra by climbing up the polyad ladder, one polyad after the other. Each time a new polyad is studied, the terms that are added to the effective hamiltonian consist, in principle, in smaller contributions accounting for vibrational corrections of the lower polyad terms.
2. Moreover, this approach is well suited to *global analyses* of a series of polyads, leading to a *unique parameter set* for the whole set of molecular levels. To give a simple example to illustrate this concept, when fitting *simultaneously* a series of polyads  $P_0, P_1, P_2, P_3, \dots$ , the rotational constant  $B_0$  is determined through the data from all the polyads. It is the parameter of the  $J^2$  term in  $\tilde{\mathcal{H}}_{\{P_0\}}$ . All other parameters associated to  $J^2$  terms in  $\tilde{\mathcal{H}}_{\{P_{k>0}\}}$  correspond to variations of the rotational constant relative to  $B_0$  for the vibrational sublevels under consideration (that is, to quantities like  $B_v - B_0$ ).
3. Performing a global fit in this way, the parameters of any of the lowest polyads contributions  $\tilde{\mathcal{H}}_{\{P_k\}}$  are not only determined by  $P_k$  experimental data sets, but also by all  $P_{k' > k}$  experimental data sets that are included in the fit (but *not* by the  $P_{k' < k}$  experimental data sets), up to an extent depending, of course, on the order of development used for the upper polyads. For instance, as we will show later in the analysis part, in a global analysis of the  $P_0$

to  $P_3$  polyads,  $P_1$  (Dyad) parameters are determined by  $P_2$  (Pentad) and  $P_3$  (Octad) data (but not by  $P_0$  (GS) data). Therefore, each time a new polyad is considered, it is not wise to study it alone, but rather to include it in a new global analysis with the whole parameter set being refined.

Two important additional remarks should be kept in mind; they are common to any spectroscopic analysis (whichever formalism is used) but it is useful to recall these points here:

- Only *effective* hamiltonian parameters can be determined by fitting experimental data. In order to perform a spectroscopic analysis, the effective hamiltonian (as the one defined above) can be directly expanded with the correct form (simply by

ignoring inter-polyad interaction terms) and it is not necessary to explicitly perform the contact transformation which links it to the “exact” (untransformed) hamiltonian.

- However, when trying to recover molecular parameters (e.g. potential surface parameters) from the results of a rovibrational analysis, it becomes necessary to perform the contact transformation analytically, or, in other words, to determine explicitly which *reduction* has been used when analyzing the experimental data. In complex systems such as methane polyads, this can be an extremely hard task. A numerical transformation is also possible and its nature has been discussed for a special (Fermi resonance) part of the hamiltonian in [45].

The present work being dedicated to the simultaneous analysis of cold and hot bands implying polyads  $P_0$  to  $P_3$  of  $^{12}\text{CH}_4$ , we will thus use the following effective hamiltonian:

$$\begin{aligned}\tilde{H}^{(\text{Octad})} &= \tilde{H}_{\{P_0\}}^{(P_3)} + \tilde{H}_{\{P_1\}}^{(P_3)} + \tilde{H}_{\{P_2\}}^{(P_3)} + \tilde{H}_{\{P_3\}}^{(P_3)} \\ &= \tilde{H}_{\{\text{GS}\}}^{(\text{Octad})} + \tilde{H}_{\{\text{Dyad}\}}^{(\text{Octad})} + \tilde{H}_{\{\text{Pentad}\}}^{(\text{Octad})} + \tilde{H}_{\{\text{Octad}\}}^{(\text{Octad})}.\end{aligned}\quad (9)$$

Matrix elements of the effective hamiltonian are calculated in a coupled rovibrational basis using the Wigner–Eckart theorem and uncoupling tensorial relations [99]. The initial rovibrational basis set is defined as

$$|\Phi_{\text{rvr}}\rangle = \left| \left( \Psi_r^{(J,nC_r)} \otimes \Psi_v^{(s)C_v} \right)_\sigma^{(C)} \right\rangle. \quad (10)$$

**Table 3**

Number of parameters in the effective hamiltonian for the different orders. Numbers in parentheses indicate the number of fitted parameters in each case; non-fitted parameters are fixed to zero.

Order	$\tilde{H}_{\{\text{GS}\}}^{(\text{Octad})}$	$\tilde{H}_{\{\text{Dyad}\}}^{(\text{Octad})}$	$\tilde{H}_{\{\text{Pentad}\}}^{(\text{Octad})}$	$\tilde{H}_{\{\text{Octad}\}}^{(\text{Octad})}$	$\tilde{H}_{\{\text{Octad}\}}^{(\text{Octad})}$
0	1 (1)	2 (2)	2 (2)	0 (0)	5 (5)
1	0 (0)	2 (2)	5 (5)	0 (0)	7 (7)
2	2 (2)	6 (5)	21 (19)	13 (13)	42 (39)
3	0 (0)	6 (6)	35 (28)	57 (49)	98 (83)
4	3 (3)	13 (12)	71 (59)	183 (152)	270 (226)
5	0 (0)	11 (9)	94 (75)	342 (282)	448 (366)
6	4 (4)	22 (17)	0 (0)	0 (0)	26 (21)
Total	10 (10)	62 (53)	228 (188)	596 (496)	896 (747)

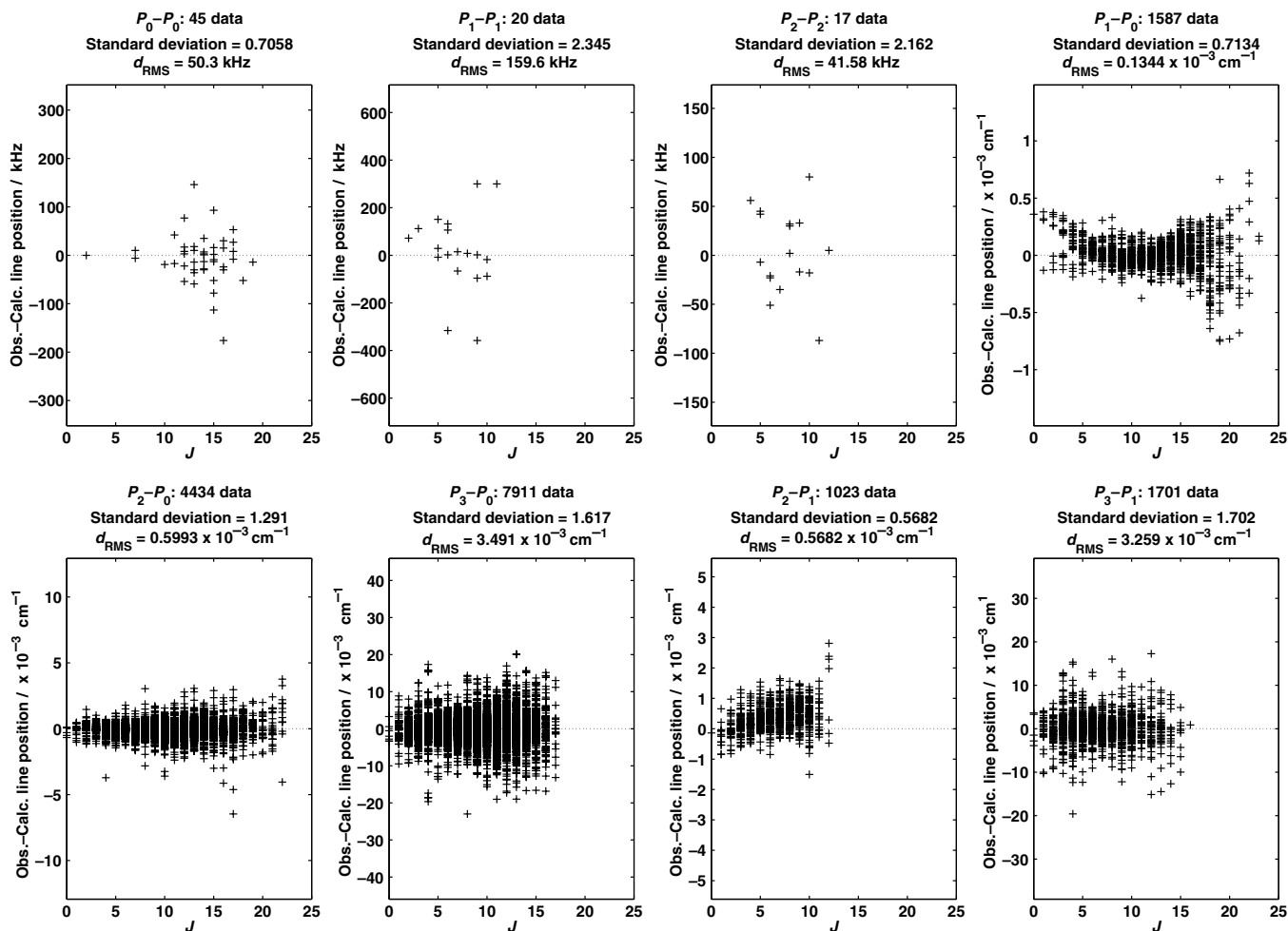


**Fig. 3.** Observed–calculated line positions and fit statistics for the different transitions studied.

$\Psi_{\sigma_v}^{(J,n_{C_v})}$  is a symmetrized rotational function while  $\Psi_{\sigma_v}^{(\{s\}C_v)}$  is a coupled vibrational basis containing the functions relevant for 4 normal modes of vibration,

$$\left| \Psi_{\sigma_v}^{(\{s\}C_v)} \right\rangle = \left| \left( \left( \Psi_{\nu_1}^{(A_1)} \otimes \Psi_{\nu_2}^{(l_2,C_2)} \otimes \Psi_{\nu_3}^{(l_3,n_3C_3)} \right)^{(C_{23})} \otimes \Psi_{\nu_4}^{(l_4,n_4C_4)} \right)^{(C_v)} \right\rangle_{\sigma_v}. \quad (11)$$

Here,  $l_2$ ,  $l_3$  and  $l_4$  are the usual vibrational angular momentum quantum numbers for degenerate vibrations and  $n_3$  and  $n_4$  are multiplicity indexes.

The effective hamiltonian matrix is diagonalized numerically, and this leads to eigenfunctions obtained from

$$\tilde{H}^{eff} \left| \Psi_{\sigma}^{J,C,\alpha} \right\rangle = E \left| \Psi_{\sigma}^{J,C,\alpha} \right\rangle, \quad (12)$$

where  $\alpha = 1, 2, \dots$  numbers functions with the same symmetry  $C$  in a given  $J$  block. It should be noticed that  $n$ , the polyad number,  $J$  and  $C$  are, strictly speaking, the only *true quantum numbers* disregarding hyperfine interactions.  $\alpha$  has no particular physical meaning. It is subject to fluctuations in the case of closely lying levels with same  $n$ ,  $J$  and  $C$ . Moreover, when considering a complex polyad with strong couplings, the assignment of a level to a given vibration can only be realized through projection onto the initial basis (Eq. 10); if the mixing between many levels becomes substantial, such an assignment becomes meaningless.

### 3.3. Tensorial model for the dipole moment

In order to calculate transition intensities (in the case of infrared absorption spectroscopy), the effective electric dipole moment operators are expanded using the same principles as discussed above. The laboratory-fixed frame (LFF) components ( $\Theta = X, Y$  and  $Z$ ) of the effective dipole moment  $\mu$  are expressed as [96,97]:

$$\tilde{\mu}_{\Theta}^{(A_2)} = \sqrt{3} \sum_m \langle 1; m | \Theta \rangle \sum_{\{i\}} \sum_{\Gamma} \mu^{(i)} \left[ C^{(1,F_1)} \otimes M^{(\{i\},F_2)} \right]^{(A_2)}. \quad (13)$$

The  $\langle 1; m | \Theta \rangle$  are Stone coefficients [106],  $C^{(1,F_1)}$  is the direction cosines tensor and  $\{i\}$  denotes all the intermediate quantum numbers and symmetries. The  $\mu^{(i)}$  are the parameters to be fitted using experimental intensity measurements. The untransformed and effective dipole moment operators are linked together through the same transformation that leads to the effective hamiltonian and this transformation is necessarily a sum of rovibrational operators [96]. Thus  $\tilde{\mu}$  is expanded in terms of rovibrational operators

$$M_{\gamma}^{(\{i\},F_2)} = \left( R^{Q(K,n\Gamma_r)} \otimes \varepsilon V_{\{s\}\{s'\}}^{\Gamma_v \Gamma_{v'}(C_v)} \right)_{\gamma}^{(F_2)}, \quad (14)$$

where  $\gamma = x, y, z$  are the molecule-fixed frame (MFF) components, with

$$\varepsilon = (-1)^Q. \quad (15)$$

In this case, the order of the development is defined as

$$\mathcal{O}_{\mu} = \Omega + \Omega_v - 1. \quad (16)$$

The vibrational extrapolation presented above also plays a role in this way of expanding the dipole moment. It allows the simultaneous analysis of cold and hot bands in a given spectral region. To illustrate this concept, let us look at the example of the Dyad region that will be considered in the intensity analysis part. For the Dyad-GS cold transitions, we have a dipole moment operator which can be symbolically written as

$$\tilde{\mu}^{(\text{Dyad-GS})} = \tilde{\mu}_{\{\text{Dyad-GS}\}}^{(\text{Dyad-GS})}. \quad (17)$$

For the Pentad-Dyad hot transitions, which lie, of course, in the same spectral region, we have:

$$\tilde{\mu}^{(\text{Pentad-Dyad})} = \tilde{\mu}_{\{\text{Dyad-GS}\}}^{(\text{Pentad-Dyad})} + \tilde{\mu}_{\{\text{Pentad-Dyad}\}}^{(\text{Pentad-Dyad})}. \quad (18)$$

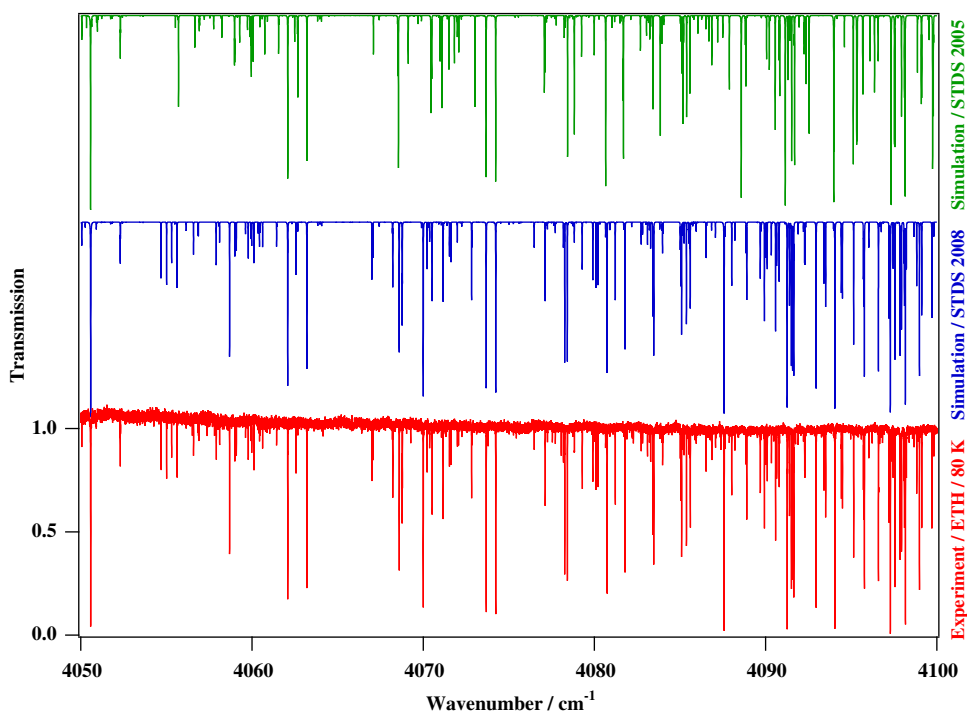


**Fig. 4.** Detail of the high-resolution absorption spectrum of the Octad region recorded at ETH Zürich at 78 K (see text for experimental details), compared to the present simulation (STDS 2008) and to the previously published results [59] as they are included in the 2005 version of the STDS database [100] (color online). (For interpretation of the references to color in this figure legend, the reader is referred to the web version of this article.)



But in this expression, we have:

$$\tilde{\mu}_{\{\text{Dyad-GS}\}}^{(\text{Pentad-Dyad})} \equiv \tilde{\mu}_{\{\text{Dyad-GS}\}}^{(\text{Dyad-GS})}. \quad (19)$$

In other words, in first approximation Dyad–GS and Pentad–Dyad intensities share the same dipole moment parameters, the term  $\tilde{\mu}_{\{\text{Pentad-Dyad}\}}^{(\text{Pentad-Dyad})}$  representing hot band specific terms of higher order. In this case, it is thus wise to analyse Dyad–GS and Pentad–Dyad intensities simultaneously.

In the Pentad and Octad regions, we only considered here cold transition intensities, because of the lack of hot band measurements, that is we used the effective dipole moments

$$\tilde{\mu}^{(\text{Pentad-GS})} = \tilde{\mu}_{\{\text{Pentad-GS}\}}^{(\text{Pentad-GS})} \quad (20)$$

and

$$\tilde{\mu}^{(\text{Octad-GS})} = \tilde{\mu}_{\{\text{Octad-GS}\}}^{(\text{Octad-GS})}. \quad (21)$$

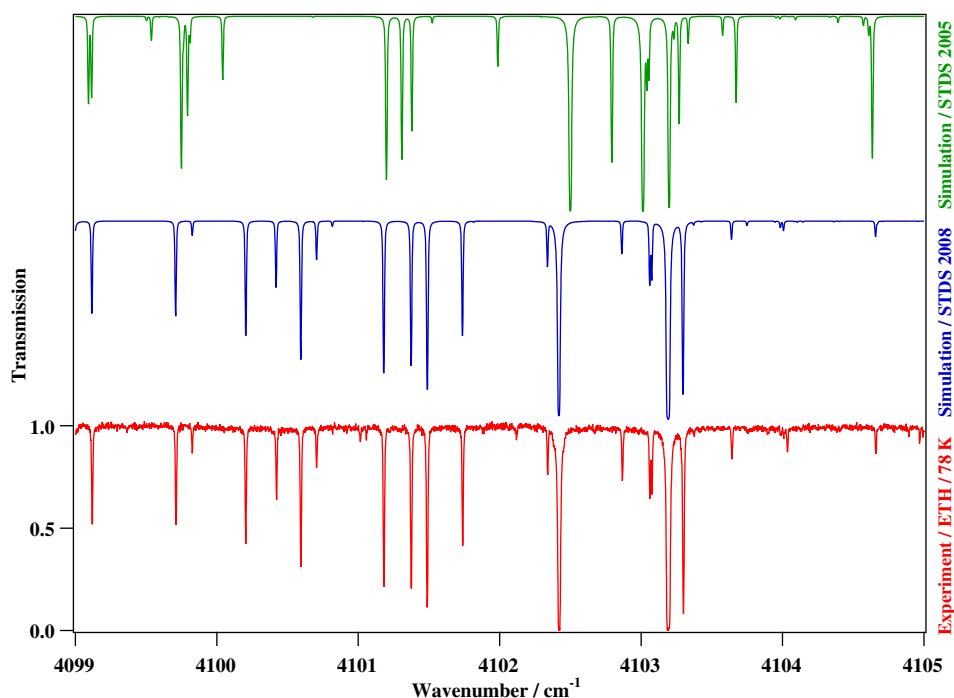


**Fig. 5.** Detail of the high-resolution absorption spectrum of the Octad region recorded at ETH Zürich at 78 K (see text for experimental details), compared to the present simulation (STDS 2008) and to the previously published results [44] (color online). (For interpretation of the references to color in this figure legend, the reader is referred to the web version of this article.)

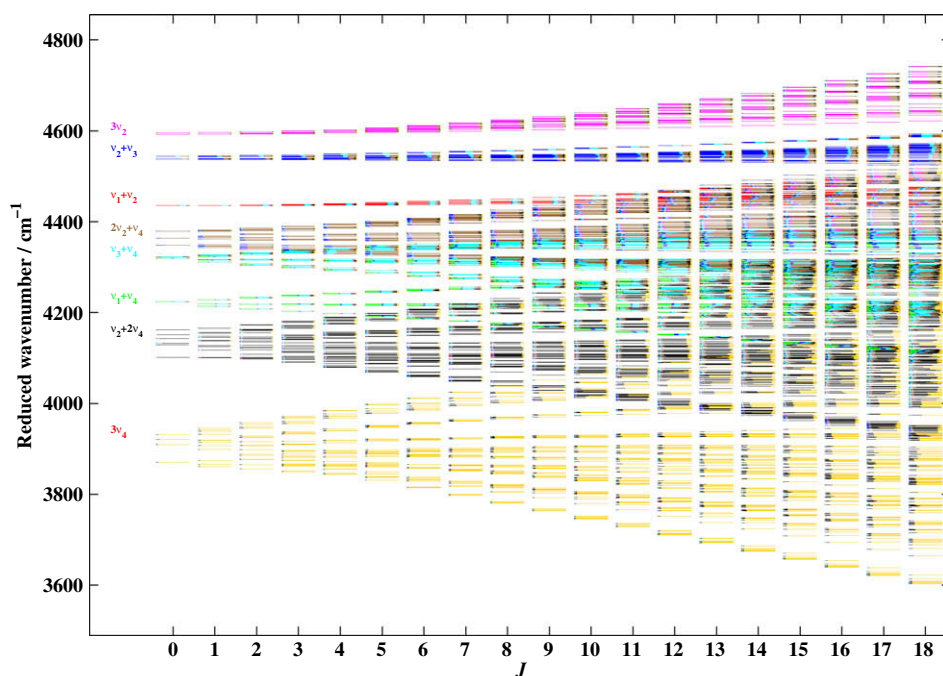


**Fig. 6.** Calculated reduced energy levels (see text) for the Octad. The colors indicating the mixings of the different normal vibrations where obtained through projection on the initial basis set (color online). (For interpretation of the references to color in this figure legend, the reader is referred to the web version of this article.)

We finally recall that the intensity  $S_{fi}$  of the dipole transition between the molecular rovibrational states  $\tilde{\Phi}_i$  (with energy  $E_i$ ) and  $\tilde{\Phi}_f$  (with energy  $E_f$ ) is calculated through

$$S_{fi} = K_{if} g_i e^{-\frac{hcE_i}{kT}} \sum_{M_i, M_f} \left| \langle \tilde{\Phi}_i | \hat{\mu}_Z | \tilde{\Phi}_f \rangle \right|^2, \quad (22)$$

where  $K_{if}$  is a numerical coefficient depending on the transition frequency  $\tilde{\nu}_{fi}$  and on the temperature  $T$  through the partition function  $Q(T)$ ; it also includes correction  $I_\alpha$  to 100%  $^{12}\text{CH}_4$  abundance:

$$K_{fi} = \frac{8\pi^3}{hc} \frac{I_\alpha}{4\pi\epsilon_0} \frac{\tilde{\nu}_{fi}}{Q(T)} \left( 1 - e^{-\frac{hc\tilde{\nu}_{fi}}{kT}} \right). \quad (23)$$

$g_i$  is the spin statistical weight of state  $\tilde{\Phi}_i$ . The sum is realized over the spherical components  $M_i$  and  $M_f$  of the two states in the LFF. Line intensities are expressed in a variety of units [107]. We used here  $\text{cm}^{-2} \text{atm}^{-1}$  at 296 K. This can be related to the fundamental integrated absorption cross section  $G_{fi} = \int \sigma_{fi}(\tilde{\nu}) \tilde{\nu}^{-1} d\tilde{\nu}$  following [79] where  $\sigma_{fi}$  is the measurable absorption cross section for the transition  $i \rightarrow f$ . Concerning the relation of the effective and true di-

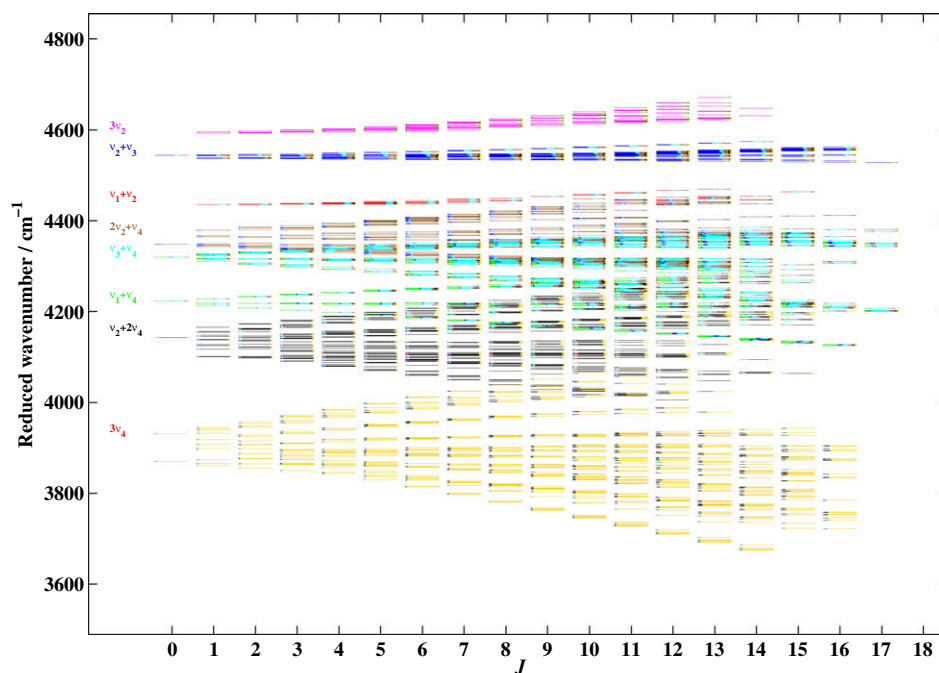


**Fig. 7.** Observed reduced energy levels reached by observed Octad-GS transitions (color online, see Figure 6 for the definition of colors). (For interpretation of the references to color in this figure legend, the reader is referred to the web version of this article.)

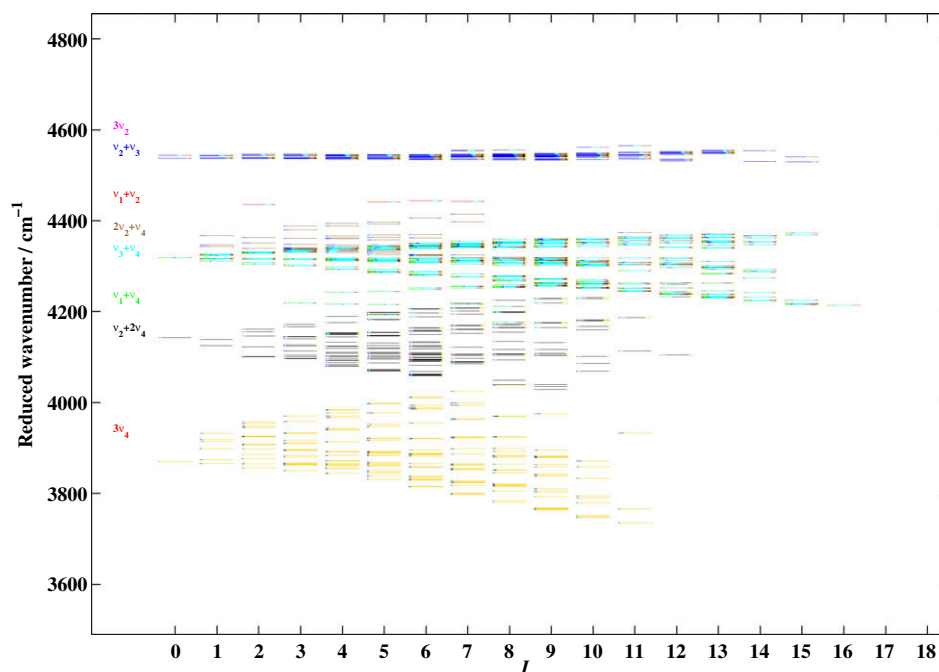


**Fig. 8.** Observed reduced energy levels reached by observed Octad-Dyad transitions (color online, see Figure 6 for the definition of colors). (For interpretation of the references to color in this figure legend, the reader is referred to the web version of this article.)

**Table 4**

Number of parameters in the effective dipole moment for the different transitions and orders. Numbers in parentheses indicate the number of fitted parameters in each case; non-fitted parameters are fixed to zero.

Order	$\tilde{\mu}_{\text{Dyad-GS}}^{(\text{Pentad-Dyad})}$	$\tilde{\mu}_{\text{Pentad-Dyad}}^{(\text{Pentad-Dyad})}$	$\tilde{\mu}_{\text{Pentad-GS}}^{(\text{Pentad-GS})}$	$\tilde{\mu}_{\text{Octad-GS}}^{(\text{Octad-GS})}$
0	1 (1)	0 (0)	1 (1)	3 (3)
1	2 (2)	3 (3)	3 (3)	12 (12)
2	4 (4)	17 (16)	9 (9)	29 (27)
3	0 (0)	0 (0)	16 (16)	51 (38)
Total	7 (7)	20 (19)	29 (29)	95 (80)

pole moments [9] the discussion follows the one on potentials. It should be emphasized that our tensorial formulation ensures a full consistency between the effective hamiltonian and the effective transition moments. Not only the formal expressions but also the numerical values of effective transition moment parameters are consistent with the effective hamiltonian and its implicit reduction (see Section 5 hereafter).

#### 4. Analysis of line positions

$\tilde{H}_{\text{GS}}^{(\text{Octad})}$ ,  $\tilde{H}_{\text{Dyad}}^{(\text{Octad})}$ ,  $\tilde{H}_{\text{Pentad}}^{(\text{Octad})}$  and  $\tilde{H}_{\text{Octad}}^{(\text{Octad})}$  were expanded up to order 6, 6, 5 and 5, respectively. In previous works,  $\tilde{H}_{\text{Pentad}}^{(\text{Octad})}$  [58] and  $\tilde{H}_{\text{Octad}}^{(\text{Octad})}$  [59] were expanded up to order 4 only, except in [44] in

which order 5 was used for the Octad. Compared to [59], we thus used an effective hamiltonian with 94 additional parameters for the Pentad and 343 additional parameters for the Octad.

As already mentioned, we performed a simultaneous analysis of the Ground State, the Dyad, the Pentad and the Octad, refining the effective hamiltonian parameters for these four polyads using all the available data cited in Section 2. Although our traditional format for tetrahedral molecule parameters is that used in the STDS software [100], for the present study we performed most of the analysis using the MIRS software [108,98] since, at the present time, this one implements a much more powerful fit algorithm than STDS; this is especially useful when dealing with complex polyad systems and a large number of parameters. The relation between MIRS and STDS parameters is not completely straightforward to establish (this would require literal algebraic expansion of all vibrational operators in both approaches). Instead, once the MIRS fit was complete, we simply used the assignment files and a partial parameter translation as a starting point for an STDS fit. All parameters except for the  $3\nu_4$  (band and its interactions) were converted exactly (because of limitations in the conversion program). Then these were held fixed and  $3\nu_4$  fitted. Energy levels obtained from both programs were the same to within better than  $10^{-4} \text{ cm}^{-1}$ . Such an agreement between two softwares written independently represents a valuable check of the validity of both implementations.

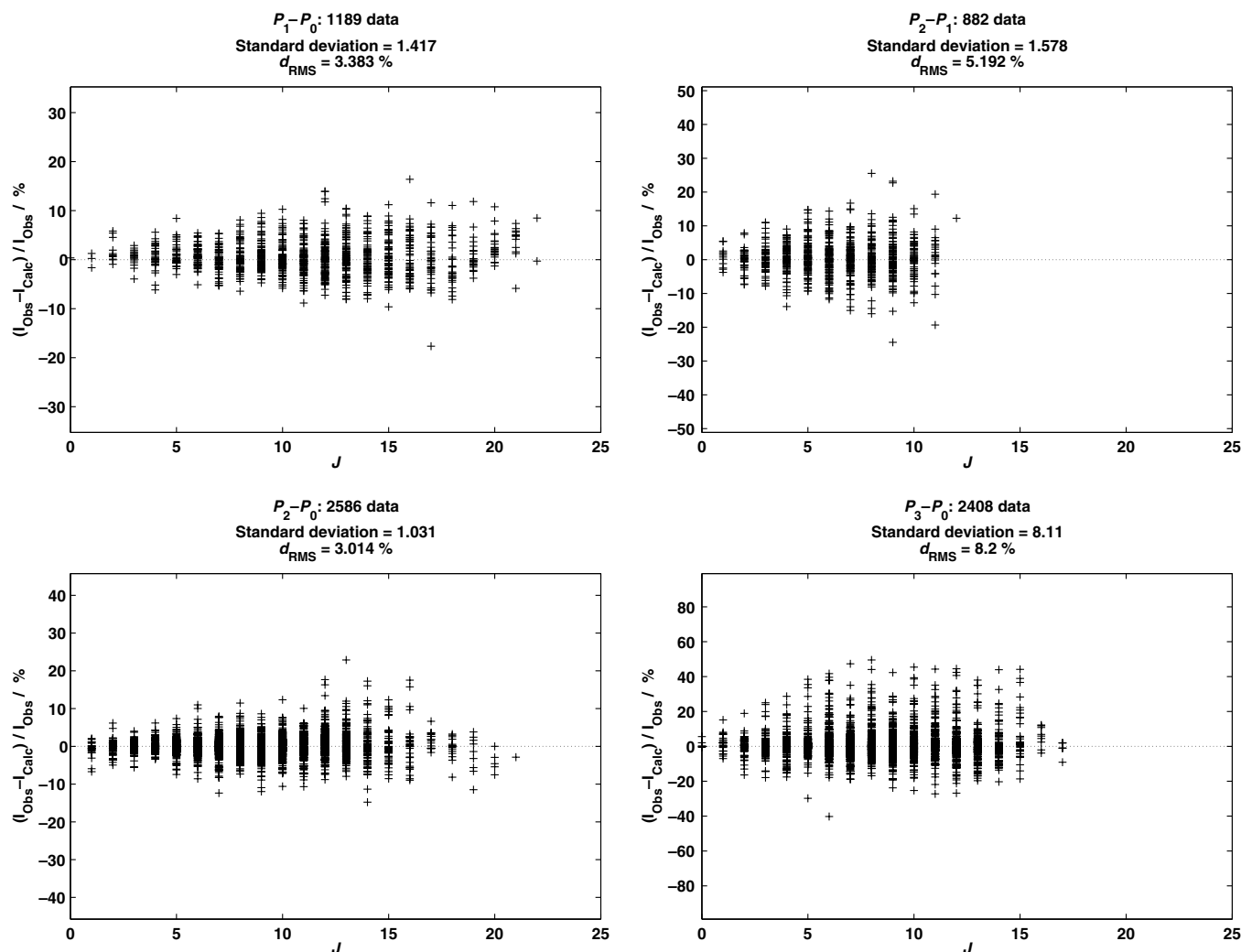


Fig. 9. Observed-calculated line intensities and fit statistics for the different transitions studied.

In this way, it was possible to obtain STDS parameters and statistics. In the following, we present the STDS results; the MIRS parameters can be obtained from the authors upon request.

Concerning assignments, we started with the list used in Ref. [59] and corrected it step by step in the Octad region. The previous Octad position assignments consisted mainly in data from the FTS spectra recorded by Brown and laser spectra recorded by Pine. In this work, 1386 new weak lines were added from the new ETH spectrum taken at 78 K. This spectrum was also used to correct erroneous assignments.

Table 3 indicates the number of parameters (total number and fitted parameters) for each order and each part of the effective hamiltonian. We used here a pragmatic approach: the non-fitted parameters are those that could not be determined (*i.e.* those leading to an uncertainty larger than the parameter itself) and that were thus fixed to zero. We did not attempt to algebraically determine the contact transformation that performs the reduction, since this would be an enormously complex task as mentioned above. A total of  $N = 16738$  experimental line positions  $\tilde{\nu}_i^e$  were used. The non-linear least-squares fit minimized the standard deviation:

$$\sigma = \sqrt{\frac{1}{N} \sum_{i=1}^N \left( \frac{\tilde{\nu}_i^e - \tilde{\nu}_i^c}{\Delta \tilde{\nu}_i^e} \right)^2}, \quad (24)$$

where the  $\tilde{\nu}_i^c$  are the calculated wavenumbers and the  $\Delta \tilde{\nu}_i^e$  the experimental uncertainties. Each experimental line positions  $\tilde{\nu}_i^e$  has the weight  $1/\Delta \tilde{\nu}_i^e$  (thus we should notice that, although they are very few, the microwave data receive a large weight because of the high precision of these measurements). Also, the lines of the cold ETH spectra have a much smaller uncertainty and thus higher weight than previous room temperature results, but the cold spectra contain fewer lines by necessity. We obtained a global  $\sigma = 1.466$ . Fig. 3 shows the observed–calculated line positions and detailed statistics for all the transitions included in the fit (as usual, for microwave transitions, the frequency  $\nu$  was used instead of the wavenumber  $\tilde{\nu}$ ). Figs. 4 and 5 show comparisons between the new ETH spectrum at 78 K in the Octad region and a simulation using

the same physical conditions, the present effective hamiltonian parameters and the effective dipole moment parameters of  $\tilde{\mu}_{i(\text{Octad-GS})}^{(\text{Octad-GS})}$  described in the next section. In Figs. 4 and 5, we also show a comparison with a simulation using the previous parameters [59] as they were implemented up to now in the STDS database; these two figures correspond to regions in which the improvement is especially striking. Compared to Ref. [59], the Octad's root mean square deviation  $d_{\text{RMS}}$  has been reduced by a factor of 11. Assignments in this region could be performed up to  $J = 18$  (instead of 16 previously). The great improvement of the new simulations compared to the previous data can be easily seen from the figures. The new simulations match experiment very closely, whereas the old data simulations show large discrepancies with experiments.

Fig. 6 shows the calculated reduced energy levels for the Octad as defined by

$$\begin{aligned} \tilde{\nu}_{\text{red}}^c &= \tilde{\nu}^c - \sum_{\Omega} t_{\{\text{GS}\}\{\text{GS}\}}^{\Omega(0,0A_1)A_1A_1} (J(J+1))^{\Omega/2} \\ &= E/hc - B_0J(J+1) + D_0J^2(J+1)^2 - \dots \end{aligned} \quad (25)$$

(this simply corresponds to the subtraction of the average rotational energy, allowing a clearer representation). The mixing between the different bands show up clearly as  $J$  increases. Figs. 7 and 8 show the “observed” energy levels (*i.e.* the levels reached by observed transitions) for the Octad–GS and Octad–Dyad transitions; this gives an idea of the sampling of the Octad's energy spectrum used in the present fit.

The full list of the 806 new effective hamiltonian parameters in STDS format are available through [supplementary material \[71\]](#).

## 5. Analysis of line intensities

Line intensities depend both on hamiltonian and dipole moment parameters. In particular, coupling parameters which induce level mixings have a large influence on intensities. Thus, the global line position fit presented above, since it has changed the effective hamiltonian parameter values, made it necessary to refit the effec-

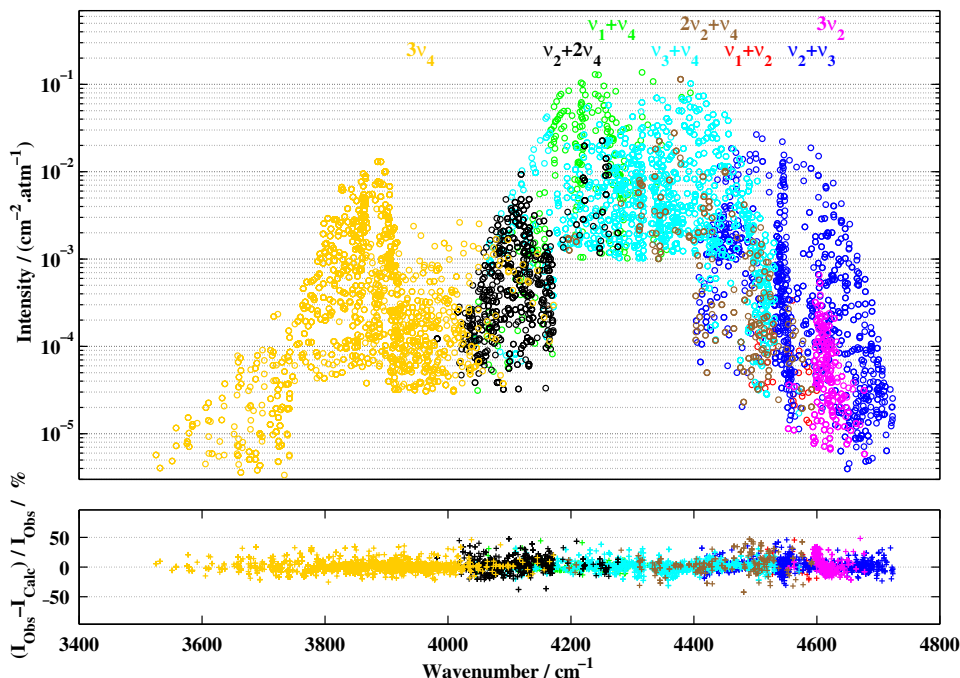


Fig. 10. Logarithmic plot of the assigned Octad–GS transition intensities (top) and intensity residuals (bottom) with the same color code as in Figure 6 (color online). (For interpretation of the references to color in this figure legend, the reader is referred to the web version of this article.)

tive dipole moment parameters. In principle, there exist several possible fit strategies when combining frequency and intensity data. In the first, one fits the line positions and line strengths in the same global fit for all hamiltonian and dipole moment operator parameters with some weighting scheme, as done for example in the case of vibrational positions and intensities in CHD<sub>3</sub> overtone spectra [45]. In the second strategy one fits first the hamiltonian parameters using line positions only and subsequently one fits the electric dipole parameters using intensity data, but keeping the hamiltonian parameters from the first step fixed. Here we used this second strategy. As mentioned in the theoretical section, Dyad–GS and Pentad–Dyad transitions were fitted simultaneously, while Pentad–GS and Octad–GS transitions were fitted separately. As in previous work [59], the same weight was applied to each experimental intensity, i.e. no attempt was made to account for a variable experimental uncertainty. The numbers of parameters used in each case are given in Table 4. Compared to [59], we expanded  $\tilde{\mu}_{\text{Octad-GS}}^{(\text{Octad-GS})}$  up to order 3 instead of 2, using thus a model with 68 additional parameters (not all of them being fitted). For Pentad–GS transitions, 4 new third order parameters were fitted (they were fixed to 0 in [58,109]). Observed–calculated intensities and detailed statistics are shown in Fig. 9 for each of the transitions studied. The root mean square deviation is defined in this case as

$$d_{\text{RMS}} = 100 \sqrt{\frac{1}{N} \sum_{i=1}^N \left( \frac{I_i^e - I_i^c}{I_i^e} \right)^2}, \quad (26)$$

where the  $I_i^e$  and  $I_i^c$  are the experimental and calculated intensities, respectively. Fig. 10 displays the intensity fit results for the Octad–GS transitions. The range of intensities used spans 5 orders of magnitude.

The new effective dipole moment parameters in STDS format are given as Supplementary material [71]. The changes compared to previous parameters are not very large.

## 6. Discussion

In Table 5, we give the positions of the vibrational levels for the Dyad, the Pentad and the Octad of <sup>12</sup>CH<sub>4</sub>. They are obtained by calculating the  $J = 0$  levels using the effective hamiltonian parameters obtained in the present study. The results are compared with the previous ones, published in Ref. [44] and with theoretical results [12,63,64]. In each case, the levels are identified by their main projection on the initial normal mode vibrational basis defined in Eq. (11) given as a percentage. In the Pentad region the differences in the largest projection hardly changed between prior and present

**Table 5**

Vibrational levels for the Dyad, the Pentad and the Octad of <sup>12</sup>CH<sub>4</sub>. The percentage corresponds to the biggest projection on the initial normal mode basis set.

Level	From Ref. [44]		This work		From Ref. [12]
$ P_n, i\rangle =  [\nu_1(0, 0A_1) \otimes \nu_2(l_2, 0C_2) \otimes \nu_3(l_3, n_3C_3)]C_{23} \otimes \nu_4(l_4, n_4C_4)]C_v\rangle^a$	$\bar{\nu}/\text{cm}^{-1}$	%	$\bar{\nu}/\text{cm}^{-1}$	%	$\bar{\nu}/\text{cm}^{-1b}$
<b>Dyad</b>					
$ P_1, 1\rangle =  [[0(0, 0A_1) \otimes 1(1, 0E) \otimes 0(0, 0A_1)]E \otimes 0(0, 0A_1)]E\rangle$	1533.336	100	1533.333	100	1533.25
$ P_1, 2\rangle =  [[0(0, 0A_1) \otimes 0(0, 0A_1) \otimes 0(0, 0A_1)]A_1 \otimes 1(1, 0F_2)]F_2\rangle$	1310.762	100	1310.761	100	1311.74
<b>Pentad</b>					
$ P_2, 1\rangle =  [[1(0, 0A_1) \otimes 0(0, 0A_1) \otimes 0(0, 0A_1)]A_1 \otimes 0(0, 0A_1)]A_1\rangle$	2916.482	90	2916.481	92	2913.71
$ P_2, 2\rangle =  [[0(0, 0A_1) \otimes 0(0, 0A_1) \otimes 1(1, 0F_2)]F_2 \otimes 0(0, 0A_1)]F_2\rangle$	3019.493	91	3019.493	97	3013.60
$ P_2, 3\rangle =  [[0(0, 0A_1) \otimes 2(0, 0A_1) \otimes 0(0, 0A_1)]A_1 \otimes 0(0, 0A_1)]A_1\rangle$	3063.643	100	3063.646	93	3063.49
$ P_2, 4\rangle =  [[0(0, 0A_1) \otimes 2(2, 0E) \otimes 0(0, 0A_1)]E \otimes 0(0, 0A_1)]E\rangle$	3065.142	100	3065.141	100	3065.01
$ P_2, 5\rangle =  [[0(0, 0A_1) \otimes 1(1, 0E) \otimes 0(0, 0A_1)]E \otimes 1(1, 0F_2)]F_1\rangle$	2846.078	100	2846.074	100	2846.91
$ P_2, 6\rangle =  [[0(0, 0A_1) \otimes 1(1, 0E) \otimes 0(0, 0A_1)]E \otimes 1(1, 0F_2)]F_2\rangle$	2830.312	93	2830.316	97	2831.53
$ P_2, 7\rangle =  [[0(0, 0A_1) \otimes 0(0, 0A_1) \otimes 0(0, 0A_1)]A_1 \otimes 2(0, 0A_1)]A_1\rangle$	2587.040	90	2587.043	97	2589.77
$ P_2, 8\rangle =  [[0(0, 0A_1) \otimes 0(0, 0A_1) \otimes 0(0, 0A_1)]A_1 \otimes 2(2, 0E)]E\rangle$	2624.618	100	2624.618	100	2627.30
$ P_2, 9\rangle =  [[0(0, 0A_1) \otimes 0(0, 0A_1) \otimes 0(0, 0A_1)]A_1 \otimes 2(2, 0F_2)]F_2\rangle$	2614.262	98	2614.261	99	2616.24
<b>Octad</b>					
$ P_3, 1\rangle =  [[1(0, 0A_1) \otimes 1(1, 0E) \otimes 0(0, 0A_1)]E \otimes 0(0, 0A_1)]E\rangle$	4435.114	90	4435.120	68	4432.22
$ P_3, 2\rangle =  [[1(0, 0A_1) \otimes 0(0, 0A_1) \otimes 0(0, 0A_1)]A_1 \otimes 1(1, 0F_2)]F_2\rangle$	4223.466	83	4223.462	50	4221.85
$ P_3, 3\rangle =  [[0(0, 0A_1) \otimes 1(1, 0E) \otimes 1(1, 0F_2)]F_1 \otimes 0(0, 0A_1)]F_1\rangle$	4537.557	91	4537.548	77	4531.37
$ P_3, 4\rangle =  [[0(0, 0A_1) \otimes 1(1, 0E) \otimes 1(1, 0F_2)]F_2 \otimes 0(0, 0A_1)]F_2\rangle$	4543.756	84	4543.757	58	4537.82
$ P_3, 5\rangle =  [[0(0, 0A_1) \otimes 0(0, 0A_1) \otimes 1(1, 0F_2)]F_2 \otimes 1(1, 0F_2)]A_1\rangle$	4322.695	82	4322.704	79	4318.42
$ P_3, 6\rangle =  [[0(0, 0A_1) \otimes 0(0, 0A_1) \otimes 1(1, 0F_2)]F_2 \otimes 1(1, 0F_2)]E\rangle$	4322.179	83	4322.178	77	4317.59
$ P_3, 7\rangle =  [[0(0, 0A_1) \otimes 0(0, 0A_1) \otimes 1(1, 0F_2)]F_2 \otimes 1(1, 0F_2)]F_1\rangle$	4322.590	87	4322.590	94	4317.83
$ P_3, 8\rangle =  [[0(0, 0A_1) \otimes 0(0, 0A_1) \otimes 1(1, 0F_2)]F_2 \otimes 1(1, 0F_2)]F_2\rangle$	4319.213	91	4319.212	39 <sup>d</sup>	4314.23
$ P_3, 9\rangle =  [[0(0, 0A_1) \otimes 3(1, 0E) \otimes 0(0, 0A_1)]E \otimes 0(0, 0A_1)]E\rangle$	4592.037	99	4592.028	89	4591.94
$ P_3, 10\rangle =  [[0(0, 0A_1) \otimes 3(3, 0A_1) \otimes 0(0, 0A_1)]A_1 \otimes 0(0, 0A_1)]A_1\rangle$	4595.586	99	4595.503	98	4595.44
$ P_3, 11\rangle =  [[0(0, 0A_1) \otimes 3(3, 0A_2) \otimes 0(0, 0A_1)]A_2 \otimes 0(0, 0A_1)]A_2\rangle$	4595.275	100	4595.269	98	4595.17
$ P_3, 12\rangle =  [[0(0, 0A_1) \otimes 2(0, 0A_1) \otimes 0(0, 0A_1)]A_1 \otimes 1(1, 0F_2)]F_2\rangle$	4348.712	47	4348.716	39	4350.10
$ P_3, 13\rangle =  [[0(0, 0A_1) \otimes 2(2, 0E) \otimes 0(0, 0A_1)]E \otimes 1(1, 0F_2)]F_1\rangle$	4363.594	92	4363.607	84	4364.74
$ P_3, 14\rangle =  [[0(0, 0A_1) \otimes 2(2, 0E) \otimes 0(0, 0A_1)]E \otimes 1(1, 0F_2)]F_2\rangle$	4378.956	54	4378.947	46 <sup>c</sup>	4379.77
$ P_3, 15\rangle =  [[0(0, 0A_1) \otimes 1(1, 0E) \otimes 0(0, 0A_1)]E \otimes 2(0, 0A_1)]E\rangle$	4104.148	68	4101.393	83	4104.48
$ P_3, 16\rangle =  [[0(0, 0A_1) \otimes 1(1, 0E) \otimes 0(0, 0A_1)]E \otimes 2(2, 0E)]A_1\rangle$	4132.953	86	4132.861	80	4135.80
$ P_3, 17\rangle =  [[0(0, 0A_1) \otimes 1(1, 0E) \otimes 0(0, 0A_1)]E \otimes 2(2, 0E)]A_2\rangle$	4161.861	100	4161.849	98	4164.36
$ P_3, 18\rangle =  [[0(0, 0A_1) \otimes 1(1, 0E) \otimes 0(0, 0A_1)]E \otimes 2(2, 0E)]E\rangle$	4151.110	76	4151.205	89	4153.76
$ P_3, 19\rangle =  [[0(0, 0A_1) \otimes 1(1, 0E) \otimes 0(0, 0A_1)]E \otimes 2(2, 0F_2)]F_1\rangle$	4128.784	88	4128.763	88	4131.31
$ P_3, 20\rangle =  [[0(0, 0A_1) \otimes 1(1, 0E) \otimes 0(0, 0A_1)]E \otimes 2(2, 0F_2)]F_2\rangle$	4142.862	94	4142.865	86	4144.88
$ P_3, 21\rangle =  [[0(0, 0A_1) \otimes 0(0, 0A_1) \otimes 0(0, 0A_1)]A_1 \otimes 3(1, 0F_2)]F_2\rangle$	3870.492	81	3870.488	91	3874.75
$ P_3, 22\rangle =  [[0(0, 0A_1) \otimes 0(0, 0A_1) \otimes 0(0, 0A_1)]A_1 \otimes 3(3, 0A_1)]A_1\rangle$	3909.174	93	3909.201	95	3912.27
$ P_3, 23\rangle =  [[0(0, 0A_1) \otimes 0(0, 0A_1) \otimes 0(0, 0A_1)]A_1 \otimes 3(3, 0F_1)]F_1\rangle$	3920.517	95	3920.510	90	3924.09
$ P_3, 24\rangle =  [[0(0, 0A_1) \otimes 0(0, 0A_1) \otimes 0(0, 0A_1)]A_1 \otimes 3(3, 0F_2)]F_2\rangle$	3930.921	95	3930.923	91	3935.34

<sup>a</sup>  $\nu_i, l_i, n_i$  and  $C_i$  ( $i = 1-4$ ) are the number of vibrational quanta, the vibrational angular momentum quantum number, the multiplicity index and the vibrational symmetry for mode  $i$ , respectively;  $C_{23}$  is an intermediate symmetry label and  $C_v$  is the overall vibrational symmetry of the state. See also Eq. (11).

<sup>b</sup> 9-Dimension numerical calculation from an *ab initio* potential.

<sup>c</sup> The major contribution of the sublevel  $|P_3, 14\rangle$  (i.e.  $(2\nu_2, E) + \nu_4, F_2$ ) is in fact 46 % of  $|P_3, 12\rangle$  (i.e.  $(2\nu_2, A_1) + \nu_4, F_2$ ).

<sup>d</sup> The major contribution of the sublevel  $|P_3, 8\rangle$  (i.e.  $\nu_3 + \nu_4, F_2$ ) is in fact 44 % of  $|P_3, 2\rangle$  (i.e.  $\nu_1 + \nu_4, F_2$ ).



[illegible]

been the subject to a recent analysis and experimental results for the Octad exist from this work as well [110]. It would also be possible to investigate hot bands in more detail. In particular, it would be interesting to analyze intensities for many of the 16 possible Octad–Dyad hot bands in the Pentad region and perhaps even a few of the 40 possible Octad–Pentad hot bands in the Dyad region.

The present results represent a very significant improvement compared to previous studies [59]. The hamiltonian and dipole moment parameters given here should be sufficiently reliable to allow a successful (and long-awaited) analysis of further polyads such as the Tetradecad and Icosad. They would also certainly be very useful to improve the knowledge of potential energy and dipole moment surfaces of  $\text{CH}_4$  [4–9]. Already now we can extract as an example a particular property of the potential hypersurface from the present global fit up to and including the Octad: The empirical position of the global minimum defined by the  $r_e$  bond length of the CH bond in methane. We find here a “best” empirical value of  $r_e = 108.47$  pm for  $^{12}\text{CH}_4$ . This can be compared with a recent *ab initio* value of  $r_e = 108.59$  pm [111]. There have been a recent result for  $\text{CH}_2\text{D}_2$  giving  $(108.55 \pm 0.14)$  pm [112] where also an extensive discussion of variety of results was given. As was discussed there, as well as in [4,9], the differences are a signature of the “real” uncertainty of the empirical data rather than of underlying effects such as non-Born–Oppenheimer behavior. In [4,9] it was concluded from a full dimensional quantum Monte Carlo analysis on the potential hyperface to obtain an accurate empirically adjusted expectation value for  $r_0$  and consequently  $r_e$ , that such a careful analysis leads to a best estimate  $r_e = (108.6 \pm 0.2)$  pm which agrees with the above mentioned empirical values within the uncertainties. Further improvement would be possible along the same lines with a two step procedure. First, the present data can be used to obtain an improved “empirical” 9-dimensional potential hypersurface. Second, this surface can then be analyzed for  $r_e$  and for the corresponding uncertainty.

Finally, the present global analysis should advance atmospheric and planetary remote sensing in both the Pentad and Octad regions because the weaker lines of  $^{12}\text{CH}_4$  are now predicted with better certainty.

## Acknowledgments

This work was supported financially by ETH Zürich, Schweizerischer Nationalfonds, the *Conseil Régional de Bourgogne*, the LEFE-CHAT National Program of the CNRS and by RFBR (Russia) through Grant 06-05-650100. We also wish to thank the SpecMo Research Group (CNRS GDR 3152). Part of the research at the Jet Propulsion Laboratory (JPL), California Institute of Technology was performed under contracts with the National Aeronautics and Space Administration. We enjoyed discussions with Hans Hollenstein and Hans-Martin Niederer, who also reproduced the entire fit of data in the paper independently for a check.

## Appendix A. Supplementary material

Supplementary data associated with this article can be found, in the online version, at [doi:10.1016/j.chemphys.2008.10.019](https://doi.org/10.1016/j.chemphys.2008.10.019).

## References

- [1] J.H. van't Hoff, Vorlesungen über Theoretische und Physikalische Chemie, Vieweg, Braunschweig, 1898.
- [2] L. Pauling, The Nature of the Chemical Bond, second ed., Oxford University, London, 1940.
- [3] W. Kutzelnigg, Einführung in die Theoretische Chemie, Verlag Chemie, Weinheim, 1975/1978.
- [4] H. Hollenstein, R. Marquardt, M. Quack, M. Suhm, J. Chem. Phys. 101 (1994) 3588.
- [5] H. Hollenstein, R. Marquardt, M. Quack, M. Suhm, Ber. Bunsenges. Phys. Chem. 99 (1995) 275.
- [6] R. Marquardt, M. Quack, J. Chem. Phys. 109 (1998) 10628.
- [7] D.W. Schwenke, H. Partridge, Spectrochim. Acta A 57 (2001) 887.
- [8] D.W. Schwenke, Spectrochim. Acta A 58 (2002) 849.
- [9] R. Marquardt, M. Quack, J. Phys. Chem. A 108 (2004) 3166.
- [10] R. Marquardt, M. Quack, J. Chem. Phys. 95 (1991) 4854.
- [11] M. Quack, W. Kutzelnigg, Ber. Bunsenges. Physik. Chem. 99 (1995) 231.
- [12] X.-G. Wang, T. Carrington Jr., J. Chem. Phys. 119 (2003) 101.
- [13] S. Peyerimhoff, M. Lewerenz, M. Quack, Chem. Phys. Lett. 109 (1984) 563.
- [14] D.R. Garmer, J.B. Anderson, J. Chem. Phys. 86 (1987) 4025.
- [15] T.J. Lee, J.M.L. Martin, P.R. Taylor, J. Chem. Phys. 102 (1995) 254.
- [16] A. Amrein, M. Quack, U. Schmitt, J. Phys. Chem. 92 (1988) 5455.
- [17] R. Signorell, R. Marquardt, M. Quack, M.A. Suhm, Mol. Phys. 89 (1996) 297.
- [18] R. Buckingham, H. Massey, S. Tibbs, Proc. Royal Soc. London: Ser. A 178 (1941) 119.
- [19] C.A. Coulson, Trans. Faraday Soc. 38 (1942) 433.
- [20] I.M. Mills, Mol. Phys. 1 (1958) 107.
- [21] S.C. Wofsy, J.S. Muentner, W. Klemperer, J. Chem. Phys. 53 (1970) 4005.
- [22] I. Ozier, W. Ho, G. Birnbaum, J. Chem. Phys. 51 (1969) 4873.
- [23] J.K.G. Watson, M. Takami, T. Oka, J. Chem. Phys. 70 (1979) 5376.
- [24] M. Quack, Angew. Chem., Int. Ed. Engl. 28 (1989) 571.
- [25] M.J.M. Pepper, I. Shavitt, P.v. Ragué Schleyer, M.N. Glukhovtsev, R. Janoschek, M. Quack, J. Comp. Chem. 16 (1995) 207.
- [26] A. Bakasov, T.K. Ha, M. Quack, J. Chem. Phys. 109 (1998) 7263.
- [27] M. Khalil, Annu. Rev. Energy Environ. 24 (1999) 645.
- [28] P.G.J. Irwin, K. Shira, N. Bowles, F.W. Taylor, S.B. Calcutt, Icarus 176 (2005) 255.
- [29] A. Caradini, G. Filacchione, F. Capaccioni, P. Cerroni, A. Adriani, R.H. Brown, Y. Langevin, B. Gondet, Planet. Space Sci. 52 (2004) 661.
- [30] H. Tran, P.-M. Flaud, T. Gabard, F. Hase, T. von Clarmann, C. Camy-Peyret, S. Payan, J.-M. Hartmann, J. Quant. Spectrosc. Radiat. Transfer 101 (2006) 306.
- [31] L.A. Sromovsky, P. Fry, Icarus 193 (2008) 252.
- [32] G.S. Orton, T. Encrenaz, C. Leyrat, R. Puetter, A.J. Friedson, Astron. Astrophys. 473 (2007) L5.
- [33] A. Coustenis, A. Salama, B. Schulz, E. Lellouch, T. Encrenaz, S. Ott, M.F. Kessler, H. Feuchtruber, T. de Graauw, in: G.L. Pilbratt, J. Cernicharo, A.M. Heras, R. Harris (Eds.), The Promise of the Herschel Space Observatory 12–15 December 2000, vol. SP-460, Toledo, Spain, (ESA, 2001).
- [34] C.A. Griffith, P. Penteado, P. Rannou, R. Brown, V. Boudon, K.H. Baines, R. Clark, P. Drossart, B. Buratti, P. Nicholson, et al., Science 313 (2006) 1620.
- [35] A. Coustenis, A. Negrão, A. Salama, B. Schulz, E. Lellouch, P. Rannou, P. Drossart, T. Encrenaz, B. Schmitt, V. Boudon, et al., Icarus 180 (2006) 176.
- [36] A. Negrão, A. Coustenis, E. Lellouch, J.-P. Maillard, P. Rannou, B. Schmitt, C.P. McKay, V. Boudon, Planet. Space Sci. 54 (2006) 1225.
- [37] A. Negrão, M. Hirtzig, A. Coustenis, E. Gendron, P. Drossart, P. Rannou, M. Combes, V. Boudon, J. Geophys. Res. 112 (2007) E02S92.
- [38] J.A. Stansberry, J.R. Spencer, B. Schmitt, A.I. Benchkoura, R.V. Yelle, J.I. Lunine, Planet. Space Sci. 44 (1996) 1051.
- [39] V. Formisano, S. Atreya, T. Encrenaz, N. Ignatiev, M. Giuranna, Science 306 (2004) 1758.
- [40] M.R. Swain, G. Vasisht, G. Tinetti, Nature 452 (2008) 329.
- [41] H.A. Jahn, Proc. Roy. Soc. A 168 (1938) 469.
- [42] H.A. Jahn, Proc. Roy. Soc. A 168 (1938) 495.
- [43] G. Herzberg, Molecular Spectra and Molecular Structure, Volume II: Infrared and Raman Spectra, Van Nostrand, Toronto, 1945.
- [44] V. Boudon, M. Rey, M. Loëte, J. Quant. Spectrosc. Radiat. Transfer 98 (2006) 394.
- [45] M. Lewerenz, M. Quack, J. Chem. Phys. 88 (1988) 5408.
- [46] M. Quack, Mol. Phys. 34 (1977) 477.
- [47] M. Quack, J. Chem. Phys. 82 (1985) 3277.
- [48] J.T. Hougen, J. Chem. Phys. 37 (1962) 1433.
- [49] T. Oka, in: K.N. Rao (Ed.), Molecular Spectroscopy: Modern Research, Vol. II, Academic Press, New York, 1976, p. 229.
- [50] I. Ozier, M.C.L. Gerry, A.G. Robiette, J. Phys. Chem. Ref. Data 10 (1981) 1085.
- [51] W.M. Itano, I. Ozier, J. Chem. Phys. 72 (1980) 3700.
- [52] R.F. Curl, J. Mol. Spectrosc. 48 (1973) 165.
- [53] M. Oldani, A. Bauder, J.-C. Hilico, M. Loëte, J.-P. Champion, Europhys. Lett. 4 (1987) 29.
- [54] E.H. Wishnow, G.S. Orton, I. Ozier, H.P. Gush, J. Quant. Spectrosc. Radiat. Transfer 103 (2007) 02.
- [55] C. Roche, J.-P. Champion, Can. J. Phys. 69 (1991) 40.
- [56] J.-P. Champion, J.-C. Hilico, C. Wenger, L.R. Brown, J. Mol. Spectrosc. 133 (1989) 256.
- [57] D. Pieroni, N. Van-Thanh, C. Brodbeck, J.-M. Hartmann, T. Gabard, J.-P. Champion, D. Bermejo, J.-L. Domenech, C. Claveau, A. Valentin, J. Chem. Phys. 113 (2000) 5776.
- [58] J.-C. Hilico, J.-P. Champion, S. Toumi, V.G. Tyuterev, A.S. Tashkun, J. Mol. Spectrosc. 168 (1994) 455.
- [59] J.-C. Hilico, O. Robert, M. Loëte, S. Toumi, A.S. Pine, L.R. Brown, J. Mol. Spectrosc. 208 (2001) 1.
- [60] O. Robert, J.-C. Hilico, M. Loëte, J.-P. Champion, L.R. Brown, J. Mol. Spectrosc. 209 (2001) 14.
- [61] M. Hippler, M. Quack, J. Chem. Phys. 116 (2002) 6045.
- [62] L.R. Brown, J. Quant. Spectrosc. Radiat. Transfer 96 (2005) 251.
- [63] X.-G. Wang, T. Carrington Jr., J. Chem. Phys. 118 (2003) 6946.

- [64] X.-G. Wang, T. Carrington Jr., *J. Chem. Phys.* 119 (2003) 94.
- [65] C. Wenger, J.P. Champion, V. Boudon, *J. Quant. Spectrosc. Radiat. Transfer* 109 (2008) 2697.
- [66] M. Quack, *J. Phys. Chem.* 83 (1979) 150.
- [67] M. Quack, J. Troe, *Theoretical Chemistry: Advances and Perspectives* 6B (1981) 199.
- [68] S. Albert, V. Boudon, M. Hippler, M. Quack, M. Rey, unpublished results.
- [69] A. Nikitin, V. Boudon, J.P. Champion, S. Albert, S. Bauerecker, M. Quack, L.R. Brown, in: *Proceedings of the 61st International Symposium on Molecular Spectroscopy*, Columbus, Ohio, 2006, p. paper RC11.
- [70] S. Albert, S. Bauerecker, M. Quack, A. Steinlin, *Mol. Phys.* 105 (2007) 541.
- [71] See [Supplementary material](#) document including tables containing the Effective hamiltonian and dipole moment parameters, as well as the list of all observed transitions. This document may be retrieved via the journal's homepage.
- [72] S. Bauerecker, M. Taraschewski, C. Weitkamp, H. Cammenga, *Rev. Sci. Instrum.* 72 (2001) 3946.
- [73] S. Albert, K.K. Albert, M. Quack, *Trends in Optics and Photonics* 84 (2003) 177.
- [74] S. Albert, M. Quack, *ChemPhysChem* 8 (2007) 1271.
- [75] S. Albert, S. Bauerecker, M. Quack, *Proceedings of the Eighteenth Colloquium on High Resolution Molecular Spectroscopy* (Dijon) (2003) 352, paper L19.
- [76] S. Bauerecker, F. Taucher, C. Weitkamp, W. Michaelis, H. Cammenga, *J. Mol. Struct.* 348 (1995) 243.
- [77] F. Taucher, C. Weitkamp, H. Cammenga, S. Bauerecker, *Spectrochim. Acta, Part A* 52 (1996) 1023.
- [78] L.S. Rothman, D. Jacquemart, A. Barbe, D. Chris Benner, M. Birk, L.R. Brown, M.R. Carleer, J.C. Chackerian, K. Chance, L.H. Coudert, et al., *J. Quant. Spectrosc. Radiat. Transfer* 96 (2005) 139.
- [79] E.R. Cohen, T. Cvitas, J.G. Frey, B. Holmström, K. Kuchitsi, R. Marquardt, I. Mills, F. Pavese, M. Quack, J. Stohner, H.L. Strauss, M. Takami, A.J. Thor, *Quantities, Units and Symbols in Physical Chemistry*, third ed., IUPAC and Royal Society of Chemistry, RSC, Cambridge, 2007.
- [80] A. Predoi-Cross, L.R. Brown, V.M. Devi, M. Brawley-Tremblay, D.C. Benner, *J. Mol. Spectrosc.* 232 (2005) 231.
- [81] L.R. Brown, J.S. Margolis, R.H. Norton, B.D. Stedry, *Appl. Spectrosc.* 37 (1983) 287.
- [82] L.R. Brown, M. Loëte, J.C. Hilico, *J. Mol. Spectrosc.* 133 (1989) 273.
- [83] O. Ouardi, J.C. Hilico, M. Loëte, L.R. Brown, *J. Mol. Spectrosc.* 180 (1996) 311.
- [84] A.S. Pine, *J. Opt. Soc. Am.* 66 (1976) 97.
- [85] A.S. Pine, *J. Chem. Phys.* 97 (1992) 773.
- [86] I.M. Grigoriev, N.N. Filipov, M.V. Tonkov, J.-P. Champion, T. Gabard, R.L. Doucen, *J. Quant. Spectrosc. Radiat. Transfer* 74 (2002) 431.
- [87] D. Bermejo, J. Santos, P. Cancio, *J. Mol. Spectrosc.* 156 (1992) 15.
- [88] J.-M. Jouvard, Phd thesis, Dijon, 1991.
- [89] M. Oldani, M. Andrist, A. Bauder, A.G. Robiette, *J. Mol. Spectrosc.* 110 (1985) 93.
- [90] H. Dreizler, private communication, 1985.
- [91] J. Hilico, M. Loëte, J. Champion, J. Destombes, M. Bogey, J. Mol. Spectrosc. 122 (1987) 381.
- [92] C.J. Pursell, D.P. Weliky, *J. Mol. Spectrosc.* 153 (1992) 303.
- [93] M. Takami, K. Uehara, K. Shimoda, *Jpn. J. Appl. Phys.* 12 (1973) 924.
- [94] J.-P. Champion, *Can. J. Phys.* 55 (1977) 1802.
- [95] M. Loëte, *Can. J. Phys.* 61 (1983) 1242.
- [96] J.-P. Champion, M. Loëte, G. Pierre, in: K.N. Rao, A. Weber (Eds.), *Spectroscopy of the Earth's Atmosphere and Interstellar Medium*, Academic Press, San Diego, 1992, p. 339.
- [97] N. Cheblal, M. Loëte, V. Boudon, *J. Mol. Spectrosc.* 197 (1999) 222.
- [98] A. Nikitin, J.-P. Champion, V.G. Tyuterev, *J. Quant. Spectrosc. Radiat. Transfer* 82 (2003) 239.
- [99] V. Boudon, J.-P. Champion, T. Gabard, M. Loëte, F. Michelot, G. Pierre, M. Rotger, C. Wenger, M. Rey, *J. Mol. Spectrosc.* 228 (2004) 620.
- [100] C. Wenger, J.-P. Champion, *J. Quant. Spectrosc. Radiat. Transfer* 59 (1998) 471.
- [101] J. Moret-Bailly, *Cah. Phys.* 15 (1961) 237.
- [102] J. Moret-Bailly, *J. Mol. Spectrosc.* 15 (1965) 344.
- [103] B.I. Zhilinskii, *Opt. Spectrosc.* 51 (1981) 262.
- [104] J.-P. Champion, G. Pierre, F. Michelot, J. Moret-Bailly, *Can. J. Phys.* 55 (1977) 512.
- [105] M. Rey, V. Boudon, C. Wenger, G. Pierre, B. Sartakov, *J. Mol. Spectrosc.* 219 (2003) 313.
- [106] A.J. Stone, *Mol. Phys.* 29 (1975) 1461.
- [107] L.A. Pugh, K.N. Rao, in: K.N. Rao (Ed.), *Molecular Spectroscopy: Modern Research*, vol. II, Academic Press, New York, 1976.
- [108] A. Nikitin, J.-P. Champion, V.G. Tyuterev, *J. Mol. Spectrosc.* 182 (1997) 72.
- [109] L. Féjard, J.-P. Champion, J.-M. Jouvard, L.R. Brown, A.S. Pine, *J. Mol. Spectrosc.* 201 (2000) 83.
- [110] H.-M. Niederer, S. Albert, S. Bauerecker, V. Boudon, J.P. Champion, M. Quack, *Chimia* 64 (2008) 273.
- [111] J.F. Stanton, *Mol. Phys.* 97 (1999) 841.
- [112] O.N. Ulenikov, E.S. Bekhtereva, S.V. Grebneva, H. Hollenstein, M. Quack, *Mol. Phys.* 104 (2006) 3371.
- [113] M. Dang-Nhu, A.S. Pine, A.G. Robiette, *J. Mol. Spectrosc.* 77 (1979) 57.
- [114] L.R. Brown, L.S. Rothman, *Appl. Opt.* 21 (1982) 2425.
- [115] J.C. Hilico, M. Loëte, L.R. Brown, *J. Mol. Spectrosc.* 152 (1992) 229.
- [116] L.R. Brown, R.A. Toth, *J. Opt. Soc. Am. B* 2 (1985) 842.
- [117] D.J.E. Knight, G.J. Edwards, P.R. Pearce, N.R. Cross, *IEEE Trans. Instrum. Meas.* 29 (257) (1980) 0018.
- [118] C.R. Pollock, F.R. Petersen, D.A. Jennings, J.S. Wells, A.G. Maki, *J. Mol. Spectrosc.* 99 (1983) 357.
- [119] C.R. Pollock, F.R. Petersen, D.A. Jennings, J.S. Wells, A.G. Maki, *J. Mol. Spectrosc.* 107 (1984) 62.